Journal of Asian Earth Sciences 50 (2012) 27–43

Contents lists available at SciVerse ScienceDirect

Journal of Asian Earth Sciences

journal homepage: www.elsevier.com/locate/jseaes

An evolving magma chamber within extending lithosphere: An integrated geochemical, isotopic and zircon U–Pb geochronological study of the Gushan granite, eastern North China Craton

Xiao-Chun Li [a], Hong-Rui Fan [a,*], M. Santosh [b], Fang-Fang Hu [a], Kui-Feng Yang [a], Ting-Guang Lan [a], Yongsheng Liu [c], Yue-Heng Yang [a]

[a] Key Laboratory of Mineral Resources, Institute of Geology and Geophysics, Chinese Academy of Sciences, Beijing 100029, China
[b] Division of Interdisciplinary Science, Faculty of Science, Kochi University, Kochi 780-8520, Japan
[c] State Key Laboratory of Geological Processes and Mineral Resources, China University of Geosciences, Wuhan 430074, China

ARTICLE INFO

Article history:
Received 15 September 2011
Received in revised form 27 November 2011
Accepted 20 January 2012
Available online 17 February 2012

Keywords:
Mafic microgranular enclaves
Isotopically zoned K-feldspar
The Gushan granite
Eastern North China Craton

ABSTRACT

The Gushan granite, located in the Jiaobei terrane of the eastern North China Craton, carries mafic microgranular enclaves (MMEs) and zoned K-feldspar phenocrysts, and is a typical example of magma generation and evolution in an extensional setting. Here we present whole rock major and trace element geochemistry, Sr–Nd isotopes and zircon U–Pb and Hf isotope data on the granite and its enclaves. The granite was emplaced at ~120 Ma. It is high in SiO_2, $K_2O + Na_2O$, LILE and LREE, but low in MgO and HFSE. The granite are also marked by high initial $^{87}Sr/^{86}Sr$ (0.7103) and low $\varepsilon_{Nd}(t)$ (−18.5 to −18.9) and zircon $\varepsilon_{Hf}(t)$ (−16.6 to −22.0) values. These features indicate that the host granite was mainly derived from ancient North China Craton lower crust. Field, petrographic and compositional studies indicate that MMEs are products of mafic–felsic magma interactions in the generation of the granite in the relatively late magmatic history. Available data suggest that enriched lithospheric mantle was a suitable candidate for the mafic magma end-member involved in the magma interaction process. Internal Sr–Nd isotopic variations within K-feldspar phenocrysts are also evaluated to decipher the magmatic history. In spite of a protracted cooling history and evidence of subsolidus alteration, the K-feldspar phenocrysts preserve marked primary Sr–Nd isotopic variations: initial $^{87}Sr/^{86}Sr$ ratios increase from the cores (0.7100–0.7102) to rims (0.7105–0.7110), whereas $\varepsilon_{Nd}(t)$ values show decrease from the cores (−17.7 to −20.5) to rims (−21.1 to −27.0). The overall isotopic profiles across the K-feldspar phenocrysts are consistent with a continuous magma contamination process. Highly negative Nd isotopic values of some K-feldspar rims suggest that the Precambrian basement rocks in the upper crust are potential candidates for the contaminant. These results indicate that isotopic heterogeneity could be preserved within single crystal from much older, slower cooled plutonic rocks, and those isotopically zoned minerals are effective recorders of open magma system. Based on petrographic, geochemical and isotopic studies, we envisage multiple magmatic pulses, mafic–felsic magma interaction, and continuous assimilation during the formation of the Gushan granite. A model involving lithospheric thinning and mantle–crust interaction in an extensional setting is proposed to account for the generation of the Gushan granite and its enclaves.

1. Introduction

The formation and differentiation of silicic magmas within an extending lithosphere often involve open-system processes such as contamination, magma recharge and mixing, and several lines of evidence can be effectively used to decipher these events. Among these, mafic microgranular enclaves (MMEs) within many felsic igneous rocks are commonly employed to identify the signature and extent of felsic–mafic magma interactions (Eichelberger, 1975, 1980; Vernon, 1984; Holden et al., 1987; Didier and Barbarin, 1991; Waight et al., 2000, 2001; Yang et al., 2004a; Kumar and Rino, 2006; Chen et al., 2009a,b). The MMEs are generally small (cm to m scale), ovoid and relatively darker than their host granites. They are typically characterized by fine grained igneous textures, and contain acicular apatite (and sometimes zircon), suggesting rapidly cooling magmas (Wyllie et al., 1962). Most microgranular enclaves have lower SiO_2 than their host granitoid, and fall on a general straight-line trend together with their host on Harker variation diagrams. These features have been taken to indicate that MMEs represent the products of incomplete mixing or mingling of globules of more mafic melts into felsic magma. In

* Corresponding author. Tel.: +86 10 82998218; fax: +86 10 62010846.
E-mail address: fanhr@mail.igcas.ac.cn (H.-R. Fan).

1367-9120/$ - see front matter © 2012 Elsevier Ltd. All rights reserved.
doi:10.1016/j.jseaes.2012.01.016

the course of slow cooling, the enclaves undergo elemental and isotopic exchange with their host granites. However, several studies have shown that MMEs and their host granitoids could retain distinct chemical and isotopic characteristics and the contrasting compositions provide potential information on magma mixing/mingling as well as on the mechanism of production of the granitic melts (Didier and Barbarin, 1991; Yang et al., 2004a).

Isotopic heterogeneity within single crystals is also an effective tool to diagnose open magma system. Traditional bulk rock isotopic analyses may "average" the complexities created by the interplay of various isotopic reservoirs and thus mask some of the important information related to the processes and ultimate sources involved in the magma system. However, isotopic variations observed within single crystals reflect growth in an open system (Davidson et al., 1998) in which the magma changes its isotope composition in response to processes such as magma mixing and/or assimilation of crustal material. In volcanic systems, several detailed crystal-isotope stratigraphy studies (e.g., Knesel et al., 1999; Tepley et al., 1999, 2000; Davidson and Tepley, 1997; Davidson et al., 2001, 2007; Perini et al., 2003; Chadwick et al., 2007; Morgan et al., 2007; Font et al., 2008; Martin et al., 2010) have shown that crystals, especially feldspars, can act as reliable recorders of their magma source composition and of the pathways of magma interaction, and can be successfully employed to identify the end-members involved in the volcanic system.

While crystal-isotope profile has been proved to be a very powerful tool in volcanic systems, only few studies have employed this approach to plutonic systems (e.g., Cox et al., 1996; Waight et al., 2000; Halama et al., 2002; Tepley and Davidson, 2003; Gagnevin et al., 2005; Davidson et al., 2008; Alves et al., 2009). One of the reasons for the scarcity of such studies is that plutonic rocks cool slowly and are thus affected by diffusive re-equilibration associated with long-term high-temperature environments, or by variable isotopic exchange associated with hydrothermal fluids (Davidson et al., 2005, 2008; Siebel et al., 2005; Ramos and Tepley, 2008). Although Sr and Pb isotopes are relatively sensitive to such disturbances, Nd isotope is a much more "robust" tracer, given its slow diffusion rates and low mobility (Lesher, 1994; Van Orman et al., 2001; Cherniak, 2003). Therefore, multiple isotopic systems can be used in a complementary fashion in some cases to rule out the effects of both slow cooling, high-temperature alteration and/or hydrothermal isotopic resetting.

The Gushan granite, located in the Jiaobei terrane, eastern North China Craton (NCC) contains many zoned K-feldspar phenocrysts and small amount of MMEs. No detailed works have been carried out previously on these rocks. Here we present petrological, geochronological and whole-rock geochemical data on the intrusion and its MMEs in order to constrain the age, petrogenesis and magma process. Furthermore, we investigate Sr–Nd isotope signatures across zoned K-feldspar phenocryst to test whether isotopic variations can be recorded and, if so, what the implications of the results are.

2. Geological setting

The North China Craton (NCC), with an Archean core of 2.5–3.8 Ga, is the largest and oldest craton in China (Geng et al., 2012; Zhai and Santosh, 2011). Based on lithological, geochemical and metamorphic P–T–t path studies of the basement rocks, the NCC can be divided into three parts (Fig. 1): the Eastern Block, the Western Block and the Trans-North China Orogen (Zhao et al., 2001). Following cratonization at ~2.5 Ga (Zhao et al., 1998) and amalgamation of the Eastern and Western Blocks at ~1.88 Ga (Zhao et al., 2001), it remained largely quiescent from the Late Paleoproterozoic until the Mesozoic, when a number of major geological events are recorded in and adjacent to the NCC.

Jiaodong Peninsula occupies the easternmost edge of the Eastern Block of the NCC and is geologically divided into the southeastern Ludong terrane and the northwestern Jiaobei terrane by the Wulian–Yantai fault (Fig. 1). The Gushan granite studied in this work occurs within the Jiaobei terrane.

The Precambrian basement in the Jiaobei terrane is mostly defined by the Archean Jiaodong Group and the Paleoproterozoic Fenzishan and Jingshan Groups (e.g., Tang et al., 2007; Jahn et al., 2008; Tam et al., 2011). The Jiaodong Group consists mainly of tonalite–trondhjemite–granodiorite (TTG) gneiss with small amounts of supracrustal rocks and mafic granulite/amphibolite lenses. Previous geochronological and geochemical studies revealed that the TTG gneiss, amphibolite and granulite have protolith ages of ~2.9 and ~2.7 Ga, ~2.5 Ga, and ~2.4 Ga, respectively; and Nd model ages of ~3.0–2.6 Ga (Tang et al., 2007; Jahn et al., 2008). The Fenzishan and Jingshan Groups comprise schist, paragneiss, calc-silicate rocks, marble, and minor mafic granulite and amphibolite, and unconformably overly the TTG gneiss. SHRIMP zircon U–Pb dating of metasedimentary rocks of the Fenzishan and Jingshan Groups yielded variable detrital ages from 2.9 to 2.2 Ga (Wan et al., 2006).

Mesozoic magmatic rocks crop out widely in the Jiaobei terrane and two main periods of magmatism are recognized as Jurassic (Early Yanshanian) and Early Cretaceous (Late Yanshanian) (Fig. 2). The Jurassic magmatic activity is represented by the crustally-derived Linglong and Luanjiahe granitoids, emplaced from 158 to 160 Ma (Wang et al., 1998; Hou et al., 2007). In the Early Cretaceous, extensive magmatism took place, including Guojialing (126–130 Ma), Aishan (116–125 Ma) and Gushan (119 Ma, this study) granitoids, intermediate-silicic volcanic rocks (108–110 Ma), and numerous mafic dikes (122–128 Ma) (Wang et al., 1998; Fan et al., 2001; Yang et al., 2004b; Liu et al., 2009; Goss et al., 2010). This period also coincides with large-scale gold mineralization and extensional to strike-slip deformation in the Jiaobei terrane (Wang et al., 1998; Zhu et al., 2001; Fan et al., 2005). Based on field, geological and geophysical evidence, the Early Cretaceous is widely considered as the climax of destruction of the NCC keel (Wu et al., 2005a; Xu et al., 2009; Zhang et al., 2011).

The Gushan pluton is located to the east of Laizhou City (Fig. 2) and covers an area of ~20 km^2. It intrudes into the Jurassic Luanjiahe granite, and mainly consists of granite. MMEs comprise <1% of the outcrop.

3. Petrography

3.1. The Gushan granite and MMEs

The Gushan granite shows a porphyritic texture (Fig. 3a). The main mineral assemblage is K-feldspar (35–40%), plagioclase (30–35%), quartz (20–25%), hornblende (5–10%) and biotite (<5%). The accessory minerals are titanite, opaque oxides, zircon and apatite, with minor secondary sericite and calcite. K-feldspar appears mainly as euhedral phenocryst (Fig. 3b), with the largest crystal up to 3 cm in length. A detailed description of its petrography is presented in a later section. The plagioclase crystals (2–5 mm) are euhedral–subhedral and a few of them are altered to sericite and albite. Quartz grains (0.5–3 mm) are mainly anhedral. Scattered hornblende (2–4 mm) and biotite (1–2 mm) crystals are euhedral–subhedral and do not show any imprints of later hydrothermal alteration (Fig. 3c).

The MMEs within Gushan granite are generally ovoid and are centimeter to decimeter in diameter (Fig. 3a). They are fine grained and contain dominantly hornblende, plagioclase and K-feldspar,

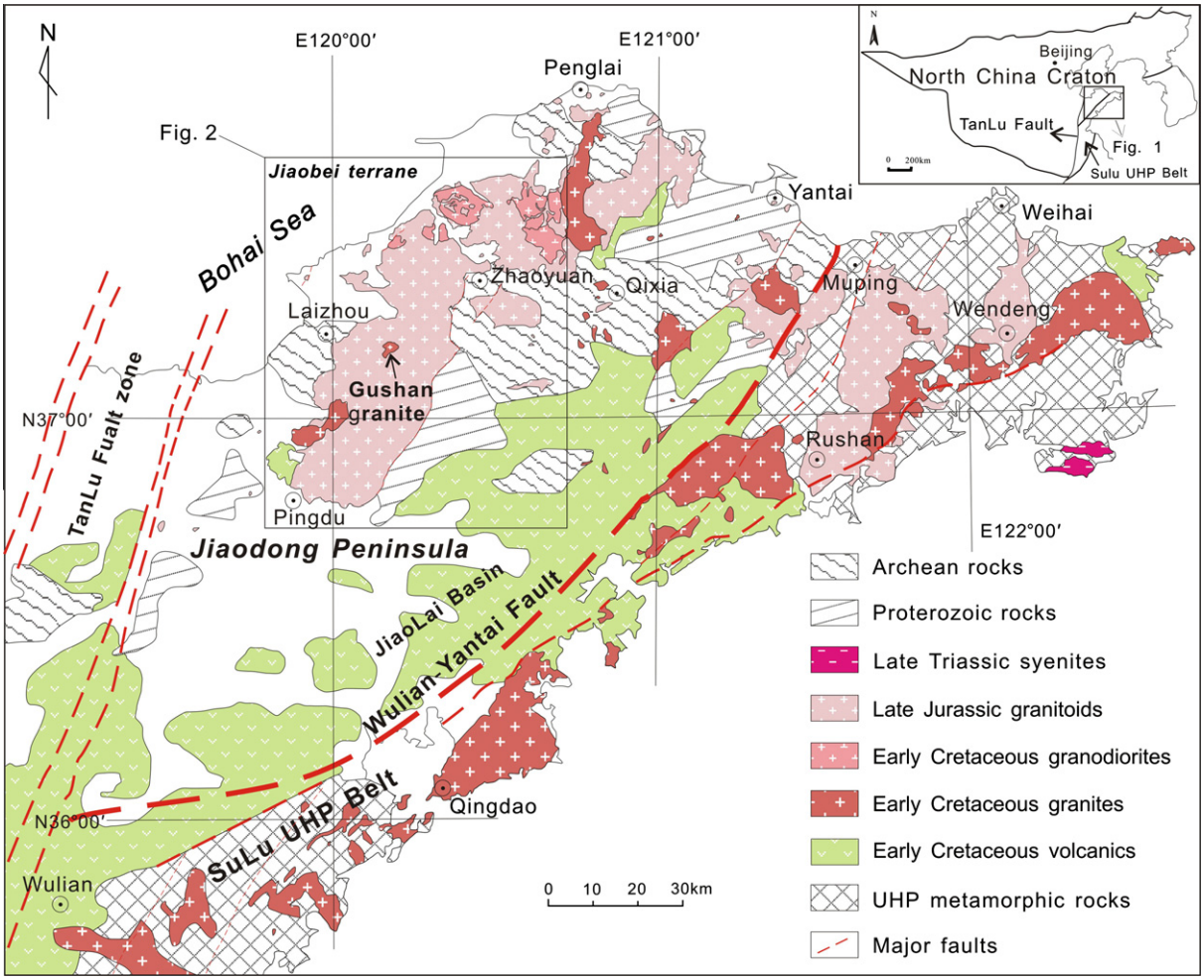

Fig. 1. Geological map of Jiaodong Peninsula showing the major tectonic units and the location of Jiaobei terrane (modified after Goss et al. (2010)).

with subordinate biotite, quartz and apatite (Fig. 3d). Some disequilibrium textures, like acicular apatite, rims of biotite on quartz ocelli, are present. K-feldspar phenocrysts which petrographically and compositionally resemble crystals from the host granite occur in the MMEs. Most of these K-feldspar phenocrysts display ovoid or irregular shape, which may correspond to dissolution in the more mafic magma. A minor proportion of these K-feldspar phenocrysts are surrounded by a thin rim of plagioclase (Fig. 3a). These features imply that K-feldspars may have been transferred from the host granitic magma into mingled more mafic melts leading to crystal-melt disequilibrium (Waight et al., 2000; Chen et al., 2009a).

3.2. K-feldspar phenocrysts

The K-feldspar phenocrysts are euhedral and generally pinkish in color in hand specimen. A few fine-scale perthites and mineral inclusions define relatively regular concentric zoning patterns (Fig. 3b).

We identified two compositional domains within the K-feldspar phenocrysts, each with distinct characteristics both in the macro- and micro-scale (Fig. 3b, e and f). The first domain is colorless and exhibits smooth non-turbid surfaces in polished thin section. These regions are characterized by fine-scale regular micro- to cryptoperthites, consisting of Ab-rich and Or-rich lamellae with a periodicity up to a few μm. The second domain shows a pink-color in hand specimen and is turbid under the microscope. A high density of coarse, irregular patch perthite coupled with the abundance of tiny pits is noted in these regions. Some pink colored fractures, filled with later carbonate, cut through the K-feldspar phenocrysts. These features are very similar to the deuterically altered K-feldspar reported in some granitoids such as the Shap granite and Klokken syenite (Worden et al., 1990; Lee and Parsons, 1997; Parsons and Lee, 2009). It is therefore considered that some parts of the K-feldspar phenocrysts were affected by deuteric alteration.

The K-feldspar phenocrysts contain minor inclusions of plagioclase, quartz and biotite. The plagioclase inclusions display features typical of magmatic growth such as zonal alignment and euhedral shape. They generally increase in both size and frequency from the core to the rim of the host phenocryst. Quartz inclusions are subhedral and appear only in the outermost rim of the host K-feldspar, which suggest that the K-feldspar rim and quartz were relatively late crystallization phases in the magma. Minor small biotite inclusions with euhedral to subhedral shape also occur.

4. Analytical methods

4.1. Cathodoluminescence (CL) images of zircon grains

CL images of zircon grains were obtained using a CAMECA SX50 electron microprobe at the Institute of Geology and Geophysics, Chinese Academy of Sciences (IGGCAS). The operating conditions were 15 kV accelerating voltage and 20 nA primary beam current.

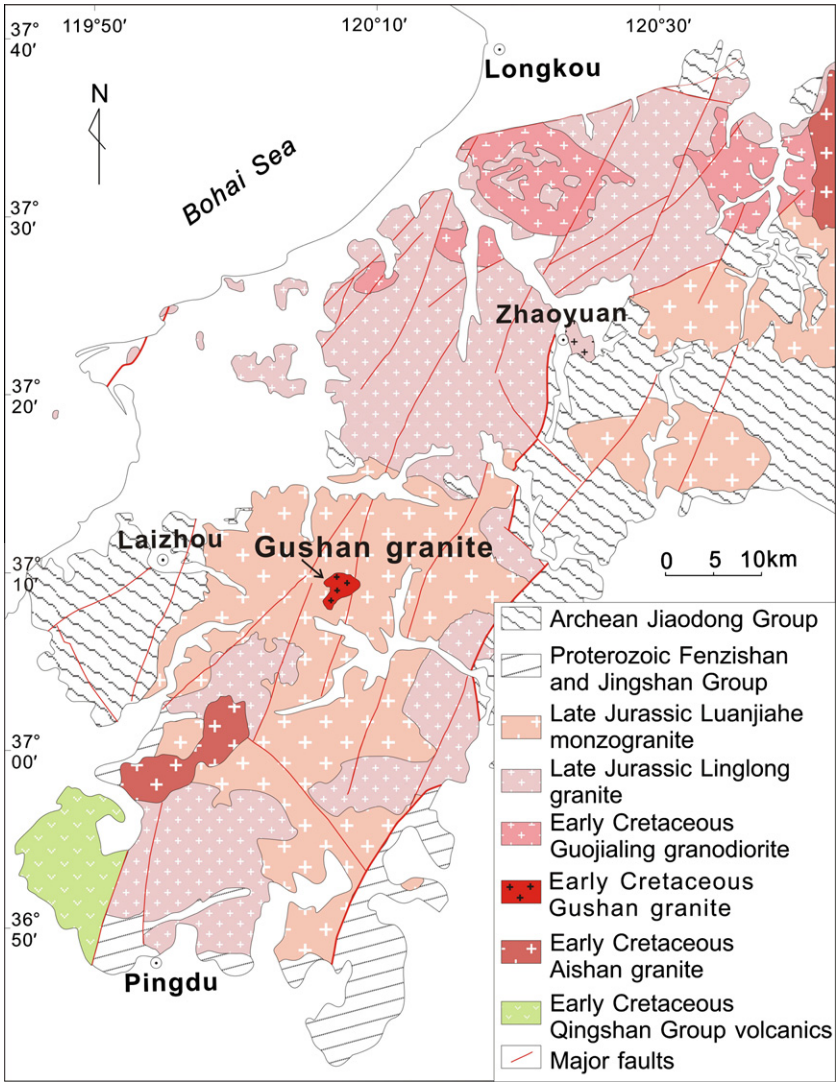

Fig. 2. Geological map of Jiaobei terrane showing the distribution of Mesozoic igneous rocks and the location of the Gushan granite (modified after Wang et al. (1998).

4.2. Major and trace elements

Major and trace elements were analyzed in the Major and Trace Elements Laboratories of IGGCAS. For major element analyses, mixtures of whole-rock powder (0.5 g) and $Li_2B_4O_7$ + $LiBO_2$ (5 g) were heated and fused into glass disks and analyzed by X-ray fluorescence spectroscopy (XRF) with an AXIOS Minerals spectrometer. The analytical uncertainties were generally within 0.1–1% (RSD). Loss on ignition (LOI) was obtained using 0.5 g powder heated up to 1100 °C for 1 h. For trace element analyses, whole-rock powders (40 mg) were dissolved in distilled HF + HNO_3 in Teflon screw-cap capsules at 200 °C for 5 days, dried, and then digested with HNO_3 at 150 °C for 1 day, and the final step was repeated. Dissolved samples were diluted to 49 ml with 1% HNO_3 and 1 ml 500 ppb indium was added to the solution as an internal standard. Trace element abundances were determined by inductively coupled plasma mass spectrometry (ICP-MS) using a Finnigan MAT ELEMENT spectrometer, which has analytical uncertainties within 5% for most elements.

4.3. Sr and Nd isotopes of whole rock

The Rb–Sr and Sm–Nd isotopic analysis followed procedures similar to those described by Chu et al. (2009a). Whole rock powders for Sr and Nd isotopic analyses were dissolved in Teflon bombs after being spiked with mixed ^{87}Rb–^{84}Sr, ^{149}Sm–^{150}Nd tracers prior to HF + HNO_3 + $HClO_4$ dissolution. Rb, Sr, Sm and Nd were separated using conventional ion exchange procedures and measured using a Finnigan MAT262 multi-collectormass spectrometer at IGGCAS. Procedural blanks are <100 pg for Rb, <300 pg for Sr, <30 pg for Sm, and <100 pg for Nd. The isotopic ratios were corrected for mass fractionation by normalizing to $^{86}Sr/^{88}Sr = 0.1194$ and $^{146}Nd/^{144}Nd = 0.7219$, respectively. The measured values for the NBS987 Sr standard and JNdi-1 Nd standard were $^{87}Sr/^{86}Sr = 0.710234 \pm 13$ (2σ, $n = 10$) and $^{143}Nd/^{144}Nd = 0.512129 \pm 14$ (2σ, $n = 10$), respectively. USGS reference material BCR-2 was measured to monitor the accuracy of the analytical procedures, with the following results: $^{87}Sr/^{86}Sr = 0.704966 \pm 11$ (2σ, $n = 12$) and $^{143}Nd/^{144}Nd = 0.512636 \pm 11$ (2σ, $n = 12$).

4.4. Sr and Nd isotopes of K-feldspar phenocryst

Because of low concentration of Nd in K-feldspar (usually < 1 ppm), we sampled a greater volume and at a relatively large spatial resolution to ensure enough material was available for the needed analytical precision. The phenocryst was cut into a 1–2 mm thick slice which allowed the core and rim of the phenocryst to be identified. Parts of individual phenocrysts, including core, mantle and rim/core and rim, were separated from the thin

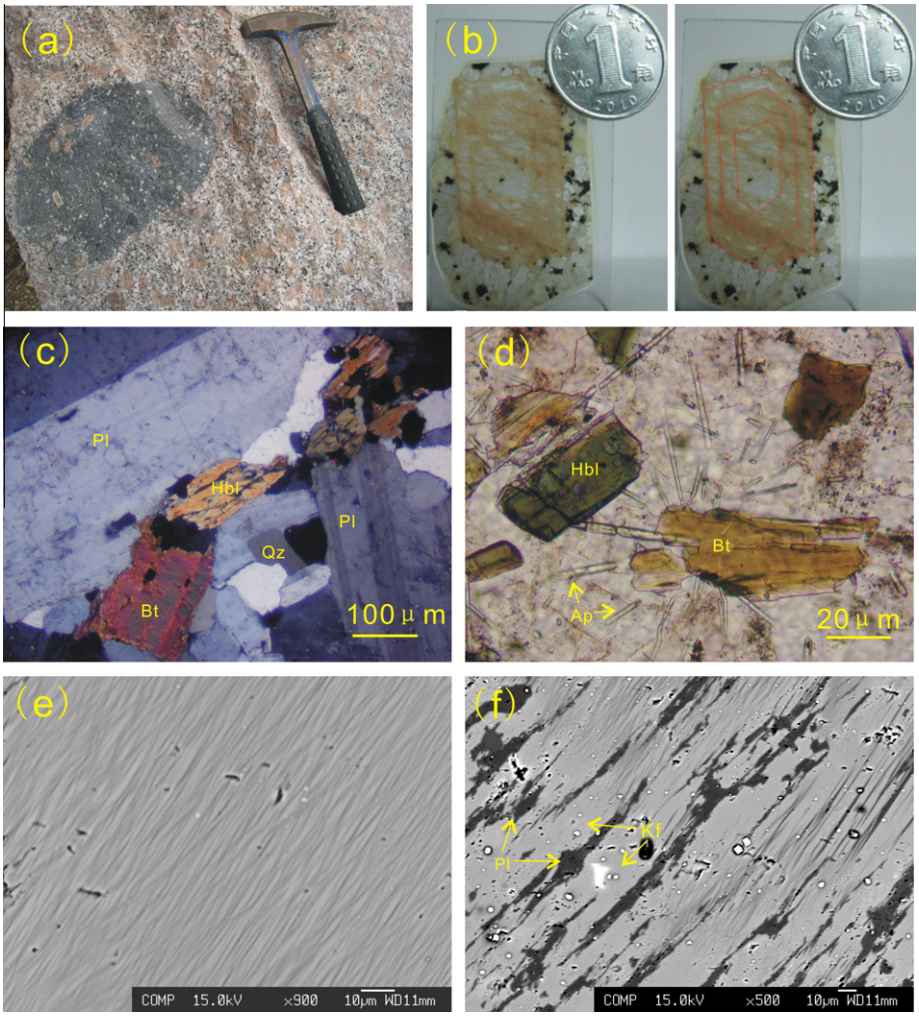

Fig. 3. (a) Field photographs of the Gushan granite and an included mafic microgranular enclave. Some ovoid K-feldspar phenocrysts appear in the enclave. (b) Polished rock slabs, showing how samples from core, mantle and rim could be separated based on the zoning patterns. Some parts of the K-feldspar phenocryst are optically colorless and transparent, whereas other areas are pink. (c) Polarized light microscope image of minerals in the matrix of the Gushan granite. Most minerals are fresh, with no characteristics of alteration. (d) Microphotograph of mafic microgranular enclaves in the granite. Note the fine-grained minerals and acicular apatite. (e) Backscattered-electron (BSE) image of the "pristine" K-feldspar phenocryst, which contains micro- to cryptoperthites. The lighter part is more potassic; the darker part is more sodic. (f) BSE image of "turbid" area within the K-feldspar phenocryst, which corresponds to patch perthite coupled with the abundance of tiny pits. Pl – plagioclase, Hbl – hornblende, Kf – K-feldspar, Qz – Quartz, Ap – apatite.

slices based on the zoning pattern within the phenocryst (Fig. 3b). Mineral inclusions and strongly altered areas were avoided during the micro-sampling. About 50–80 mg of material was crushed and handpicked under a binocular for the Sr and Nd isotopic analysis.

In interpreting the Sr–Nd isotopic data from the feldspar phenocrysts, attention was paid to the following points. Careful sampling of the individual growth zones of the K-feldspar phenocrysts was performed. The relatively wide separation of the zones and their averaged isotopic compositions were considered over a relatively large volume in the crystal. Furthermore, care was taken to sample as close to the "true" crystal core, mantle and rim as possible.

The Rb–Sr and Sm–Nd isotopic analysis followed procedures similar to those described by Chu et al. (2009b). Crushed samples were dissolved in a HF–$HClO_4$–HNO_3 mixture and spiked with appropriate amounts of mixed ^{87}Rb–^{84}Sr, ^{149}Sm–^{150}Nd tracer solution in Teflon bombs. Rb and Sr were separated using standard ion-exchange resins and measured using a Finnigan MAT 262 mass spectrometer at University of Science and Technology, China. Sm and Nd were separated using Eichrom LN (LN-C-50B, 100–150 μm, 2 ml) chromatographic columns and analyzed on an IsoProbe-T thermal ionization mass spectrometer (GV instruments, England), installed at the IGGCAS. The isotopic ratios were corrected for mass fractionation by normalizing to $^{86}Sr/^{88}Sr = 0.1194$ and $^{146}Nd/^{144}Nd = 0.7219$, respectively. The measured value for NBS987 Sr standard and JNdi-1 Nd standard were 0.710244 ± 9 (2σ, $n = 12$) and 0.512123 ± 11 (2σ, $n = 12$), respectively. Total procedural blanks are <40 pg for Rb, <300 pg for Sr, <20 pg for Sm, and <70 pg for Nd. Nd isotopic data of a few samples cannot be successfully analyzed due to the low Nd concentrations of K-feldspar. Some samples lack Sr isotopic data, resulting from inappropriate spiking or unsuccessful measurement.

4.5. Zircon U–Pb dating and in situ Hf isotopic analyses

U–Pb dating and trace element analyses of zircon were conducted synchronously by LA-ICP-MS at the State Key Laboratory of Geological Processes and Mineral Resources, China University of Geosciences, Wuhan. Detailed operating conditions for the laser ablation system, the ICP-MS instrument, and the data reduction process are described by Liu et al. (2008, 2010). Laser sampling was performed using a GeoLas 2005. An Agilent 7500a ICP-MS instrument was used to acquire ion-signal intensities. Each

analysis incorporated a background acquisition of approximately 20–30 s (gas blank) followed by 50 s data acquisition from the sample. The Agilent Chemstation was utilized for the acquisition of each individual analysis. Off-line selection and integration of background and analytical signals, time-drift correction, and quantitative calibration for trace element analyses and U–Pb dating were performed by ICPMSDataCal (Liu et al., 2008, 2010).

Zircon 91500 was used as the external standard for U–Pb dating, and was analyzed twice every five analyses. Time-dependent drifts of U–Th–Pb isotopic ratios were corrected using a linear interpolation (with time) for every five analyses according to the variations of 91500 (i.e., 2 zircon 91500 + 5 samples + 2 zircon 91500) (Liu et al., 2010). Preferred U–Th–Pb isotopic ratios used for 91500 are from Wiedenbeck et al. (1995). Uncertainty of preferred values for the external standard 91500 was propagated to the ultimate results of the samples. Concordia diagrams and weighted mean calculations were made using Isoplot/Ex ver3 (Ludwig, 2003).

In situ zircon Hf isotopic analyses were conducted on the same spots which had been analyzed for U–Pb dating. Hf isotopic compositions were determined by a Neptune MC-ICP-MS equipped with a GeolasPlus 193 nm ArF excimer laser at the IGGCAS. Laser spot size of 40 μm and laser repetition of 8 Hz with energy density of 15 J/cm^2 were used during the analysis. The signal collection model is one block with 200 cycles. Each cycle has 0.131 s integration time and total time is about 26 s during each analysis. Zircon 91500 was used as external standard for Hf isotopic analyses and was analyzed twice every five analysis. Repeated analysis of 91500 yielded a mean $^{176}Hf/^{177}Hf$ ratio of 0.282310 ± 26 (2σ, n = 82), which is consistent with the $^{176}Hf/^{177}Hf$ ratios measured by Goolaerts et al. (2004). Detailed analytical procedures were described by Xie et al. (2008).

5. Results

5.1. Geochronology

5.1.1. The Gushan granite

Zircon crystals in the Gushan granite (Sample 10G07 and 10G11) are euhedral and range from 100 to 200 μm in size, with length to width ratios ranging from 1.5:1 to 3:1. Most grains are transparent and pale yellow in color and show magmatic oscillatory zoning.

Nineteen zircons are analyzed from Sample 10G07. A $^{206}Pb/^{238}U$ vs. $^{207}Pb/^{235}U$ plot shows that all of the data are concordant, with a weighted mean $^{206}Pb/^{238}U$ age of 118.7 ± 0.9 (MSWD = 2.3) (Fig. 4a and Table 1). All seventeen zircons from Sample 10G11 are concordant and yield a mean $^{206}Pb/^{238}U$ age of 120.0 ± 1.1 Ma (MSWD = 0.93) (Fig. 4b and Table 1).

5.1.2. MMEs within the Gushan granite

Zircon crystals from MMEs within the Gushan granite (Sample 10GS20) are euhedral, transparent and pale yellow in color and range from 80 to 150 μm in size, usually with lower length to width ratios (1.5:1–2:1) than zircons from the host granite.

The seventeen zircons analyzed are concordant and yield a mean $^{206}Pb/^{238}U$ age of 118.5.7 ± 1.0 Ma (MSWD = 0.71) (Fig. 4c and Table 1), indicating coeval crystallization of the enclaves and host granite.

5.2. Whole-rock major and trace elements

The whole-rock major and trace element data are presented in Table 2.

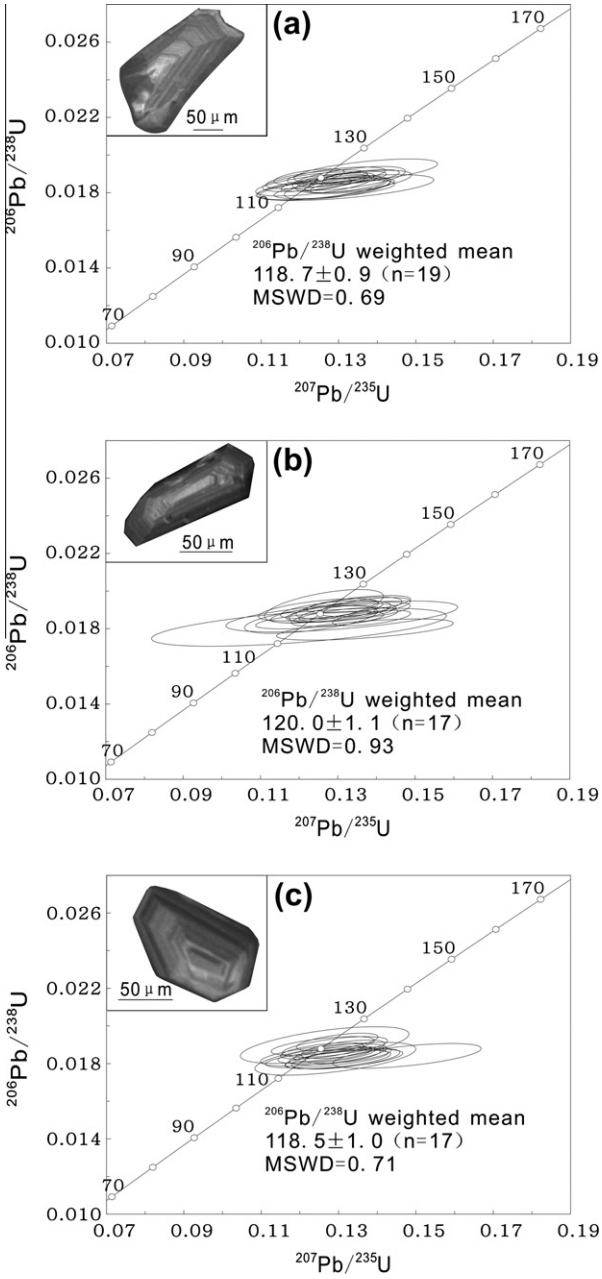

Fig. 4. LA-ICP-MS zircon U–Pb concordia of Sample 10G07 (a), Sample 10G11 (b) and Sample 10GS20 (c). The insets show typical CL images of zoned zircons.

The Gushan granite shows SiO_2 concentrations of 69.48–72.72 wt.%, falling in the domain of granite in the total alkalis vs. silica diagram (Fig 5a). The A/NK vs. A/CNK plot (Fig. 5b) shows that the granites are peraluminous. They exhibit relatively high contents of $K_2O + Na_2O$ (7.83–9.15 wt.%), but low contents of MgO (0.70–1.07 wt.%), TiO_2 (0.26–0.40 wt.%), P_2O_5 (0.11–0.51 wt.%) and Ni (9.7–12.3 ppm).

The MMEs are intermediate in composition (SiO_2: 57.55–57.91 wt.%), corresponding to monzonite in the total alkalis vs. silica diagram (Fig. 5a). They are metaluminous and have higher MgO (3.17–3.81 wt.%), TiO_2 (0.72–0.82 wt.%), Ni (23.4–41.4 ppm) and Co (16.7–17.7 ppm) contents than the host granite.

In the chondrite-normalized REE diagram (Fig. 6), all samples are marked by enrichment in LREEs (ΣLREE = 211–492 ppm), strong fractionation between LREE and HREE ($(La/Yb)_N$ = 24–99),

Table 1
LA-ICP-MS U–Pb data of zircons from the Gushan granite and mafic enclave.

Sample no.	Th (ppm)	U (ppm)	Th/U	$^{207}Pb/^{206}Pb$	1σ	$^{207}Pb/^{235}U$	1σ	$^{206}Pb/^{238}U$	1σ	$^{206}Pb/^{238}U$	1σ
Granite (10G07)											
10G07-01	380	436	0.87	0.0496	0.0026	0.1243	0.0061	0.0184	0.0002	117.7	1.5
10G07-02	298	266	1.12	0.0512	0.0040	0.1290	0.0103	0.0182	0.0003	116.1	2.1
10G07-03	180	181	0.99	0.0513	0.0049	0.1258	0.0110	0.0183	0.0004	116.7	2.8
10G07-04	332	376	0.88	0.0509	0.0027	0.1294	0.0066	0.0187	0.0003	119.3	1.6
10G07-05	399	280	1.43	0.0517	0.0038	0.1294	0.0084	0.0189	0.0003	120.8	1.9
10G07-06	416	359	1.16	0.0528	0.0026	0.1358	0.0066	0.0188	0.0002	120.4	1.6
10G07-07	251	250	1.00	0.0538	0.0053	0.1371	0.0123	0.0191	0.0004	122.3	2.7
10G07-08	433	419	1.03	0.0527	0.0039	0.1298	0.0091	0.0183	0.0004	116.6	2.5
10G07-09	224	209	1.07	0.0530	0.0041	0.1327	0.0096	0.0188	0.0004	119.8	2.6
10G07-10	409	365	1.12	0.0515	0.0053	0.1260	0.0114	0.0182	0.0004	116.4	2.5
10G07-11	193	262	0.74	0.0516	0.0055	0.1321	0.0149	0.0183	0.0005	116.7	2.9
10G07-12	374	404	0.92	0.0533	0.0030	0.1336	0.0072	0.0184	0.0003	117.3	1.7
10G07-13	471	535	0.88	0.0518	0.0025	0.1331	0.0061	0.0188	0.0002	120.0	1.5
10G07-14	436	389	1.12	0.0472	0.0024	0.1224	0.0060	0.0189	0.0003	120.4	1.7
10G07-15	403	368	1.09	0.0518	0.0026	0.1316	0.0068	0.0184	0.0003	117.6	1.7
10G07-16	271	337	0.81	0.0488	0.0036	0.1244	0.0087	0.0187	0.0003	119.5	2.1
10G07-17	200	307	0.65	0.0530	0.0042	0.1339	0.0099	0.0186	0.0004	118.7	2.5
10G07-18	200	260	0.77	0.0489	0.0041	0.1236	0.0099	0.0184	0.0004	117.6	2.4
10G07-19	186	191	0.97	0.0501	0.0041	0.1241	0.0090	0.0186	0.0003	118.7	2.2
Granite (10G11)											
10G11-01	369	408	0.90	0.0542	0.0026	0.1388	0.0067	0.0186	0.0003	118.6	1.7
10G11-02	373	263	1.42	0.0493	0.0107	0.1200	0.0252	0.0181	0.0007	115.5	4.2
10G11-03	338	311	1.09	0.0479	0.0039	0.1250	0.0103	0.0190	0.0004	121.4	2.5
10G11-04	395	280	1.41	0.0534	0.0032	0.1370	0.0078	0.0192	0.0003	122.3	2.1
10G11-05	200	208	0.96	0.0575	0.0062	0.1370	0.0151	0.0180	0.0004	114.7	2.4
10G11-06	423	344	1.23	0.0518	0.0034	0.1325	0.0083	0.0188	0.0003	120.4	2.0
10G11-07	791	301	2.63	0.0516	0.0042	0.1327	0.0106	0.0189	0.0004	120.7	2.2
10G11-08	218	294	0.74	0.0526	0.0039	0.1318	0.0091	0.0186	0.0003	119.0	2.1
10G11-09	395	359	1.10	0.0493	0.0046	0.1264	0.0102	0.0192	0.0006	122.6	3.7
10G11-10	266	282	0.94	0.0500	0.0044	0.1253	0.0110	0.0185	0.0003	117.9	2.0
10G11-11	408	285	1.43	0.0502	0.0048	0.1231	0.0114	0.0185	0.0005	118.1	3.0
10G11-12	206	283	0.73	0.0511	0.0035	0.1329	0.0090	0.0191	0.0004	122.0	2.4
10G11-13	201	236	0.85	0.0511	0.0083	0.1311	0.0198	0.0187	0.0005	119.1	3.4
10G11-14	323	376	0.86	0.0511	0.0037	0.1306	0.0087	0.0189	0.0004	120.7	2.3
10G11-15	280	347	0.81	0.0503	0.0039	0.1263	0.0090	0.0188	0.0003	119.9	2.0
10G11-16	243	311	0.78	0.0512	0.0034	0.1354	0.0089	0.0193	0.0003	123.2	1.9
10G11-17	258	278	0.93	0.0486	0.0032	0.1284	0.0088	0.0190	0.0003	121.5	2.0
Mafic enclave (10GS20)											
10GS20-01	310	269	1.15	0.0518	0.0036	0.1298	0.0091	0.0182	0.0003	116.3	2.0
10GS20-02	363	393	0.92	0.0489	0.0042	0.1261	0.0108	0.0185	0.0004	117.9	2.5
10GS20-03	157	214	0.73	0.0510	0.0057	0.1292	0.0138	0.0183	0.0006	116.6	3.6
10GS20-04	186	252	0.74	0.0498	0.0036	0.1291	0.0090	0.0189	0.0004	120.6	2.3
10GS20-05	280	306	0.91	0.0522	0.0031	0.1311	0.0071	0.0188	0.0003	119.8	2.1
10GS20-06	370	319	1.16	0.0520	0.0045	0.1269	0.0105	0.0183	0.0003	116.7	2.1
10GS20-07	216	241	0.90	0.0536	0.0043	0.1315	0.0100	0.0182	0.0003	116.5	2.2
10GS20-08	295	242	1.22	0.0589	0.0050	0.1477	0.0127	0.0184	0.0004	117.6	2.8
10GS20-09	252	256	0.98	0.0519	0.0033	0.1290	0.0078	0.0184	0.0003	117.4	1.9
10GS20-10	290	301	0.96	0.0491	0.0036	0.1259	0.0088	0.0189	0.0003	120.9	2.1
10GS20-11	252	291	0.87	0.0494	0.0028	0.1257	0.0071	0.0187	0.0003	119.3	1.8
10GS20-12	315	270	1.17	0.0493	0.0054	0.1264	0.0144	0.0190	0.0006	121.2	4.1
10GS20-13	242	255	0.95	0.0499	0.0026	0.1296	0.0070	0.0191	0.0003	122.3	1.9
10GS20-14	199	237	0.84	0.0504	0.0033	0.1269	0.0083	0.0185	0.0003	117.9	1.9
10GS20-15	229	312	0.73	0.0511	0.0027	0.1285	0.0067	0.0185	0.0003	118.2	1.7
10GS20-16	211	198	1.06	0.0535	0.0039	0.1319	0.0092	0.0183	0.0004	116.6	2.3
10GS20-17	271	300	0.90	0.0523	0.0031	0.1325	0.0074	0.0184	0.0003	117.8	1.8

flat or concave upwards MREE–HREE, and weak to moderate negative Eu anomalies ($Eu/Eu^* = 0.57–0.73$). MMEs have slightly higher REE contents than the granite.

In the primitive mantle-normalized (PM: Sun and McDonough, 1989) trace element patterns (Fig. 7), all samples show enrichment in large ion lithophile elements (LILEs, such as Rb, Sr, Ba and Pb) and light REEs, and display depletion in HFSEs, including Nb, Ta and Ti. The host granites have weak to moderate negative Ba, Nb, Ta, Ti and P anomalies, whereas the enclaves have moderate negative Ba, Nb, Ta, Ti and Sr anomalies (Fig. 7).

The Nb/Ta ratios of the granite range from 12.8 to 14.5, whereas the two microgranular enclaves show Nb/Ta ratios of 20.62–22.79 (Table 2).

5.3. Whole-rock Sr and Nd isotopic data

Sr and Nd isotopic compositions of the granite and MMEs are presented in Table 3 and are shown in a plot of $\varepsilon_{Nd}(t)$ vs. $(^{87}Sr/^{86}Sr)_i$ (initial $^{87}Sr/^{86}Sr$ ratio) in Fig. 8. The granite has uniform initial $^{87}Sr/^{86}Sr$ ratios (0.7103–0.7104) and $\varepsilon_{Nd}(t)$ (−18.6 to −18.9), whereas the MMEs have slightly lower $^{87}Sr/^{86}Sr$ ratios (0.7100–0.7101) and higher $\varepsilon_{Nd}(t)$ (−15.1 to −17.7) than the host granite.

5.4. Zircon Hf isotopes

The results from in situ Hf isotopic analyses of zircons are listed in Table 4 and shown in Fig. 9.

Table 2
Major oxides (wt.%) and trace elements (ppm) for the Gushan granite and mafic enclaves.

	10YS02 Granite	10YS03 Granite	10G07 Granite	10G09P Granite	08G46 Granite	08G47 Granite	10YS20-m Mafic enclave	10YS21 Mafic enclave
SiO_2	69.61	69.48	71.61	72.72	70.98	71.53	57.82	58.12
TiO_2	0.40	0.39	0.29	0.28	0.25	0.26	0.82	0.72
Al_2O_3	14.37	14.13	14.20	13.62	14.33	13.84	15.66	15.34
Fe_2O_3T	2.75	2.85	2.06	2.06	2.96	3.24	5.96	5.80
MnO	0.05	0.05	0.04	0.04	0.03	0.04	0.20	0.16
MgO	1.07	1.05	0.73	0.73	0.70	0.75	3.81	3.17
CaO	2.26	2.21	1.82	1.72	1.63	1.86	4.54	4.36
Na_2O	3.89	3.93	3.92	3.74	4.41	4.26	3.98	3.66
K_2O	4.16	4.03	4.53	4.35	4.74	4.21	5.11	6.50
P_2O_5	0.20	0.20	0.13	0.13	0.11	0.12	0.59	0.78
LOI	0.86	0.92	0.34	0.26	0.33	0.52	1.04	0.82
Total	99.61	99.23	99.67	99.65	100.48	100.63	99.54	99.43
$Mg^{\#}$	0.44	0.42	0.41	0.41	0.32	0.32	0.56	0.52
Cr	157	247	179	149	118	92	184	146
Co	6.5	7.4	5.4	5.0	4.4	5.5	16.7	17.7
Ni	11.3	12.3	9.9	9.7	9.4	7.5	41.4	23.5
Rb	163	150	170	146	167	164	255	317
Sr	575	534	461	542	506	480	206	237
Cs	1.5	1.3	1.1	1.3	1.3	1.4	2.8	2.3
Ba	1492	1338	944	1528	1204	1042	1207	1201
La	81	71	59	59	59	122	74	104
Ce	145	127	102	103	100	175	183	237
Pr	15	14	11	11	11	16	23	29
Nd	45	43	33	36	35	47	79	102
Sm	6.2	6.4	4.9	4.9	4.9	5.3	11.9	16.7
Eu	1.4	1.2	1.1	1.1	1.0	1.0	2.3	3.1
Gd	4.9	4.8	3.9	3.8	3.9	4.8	8.7	12.7
Tb	0.50	0.53	0.41	0.42	0.45	0.46	0.98	1.43
Dy	2.1	2.1	1.7	1.7	2.0	2.0	4.1	5.9
Ho	0.35	0.38	0.31	0.32	0.37	0.35	0.76	1.00
Er	0.97	1.03	0.89	0.91	0.98	0.93	2.06	2.56
Tm	0.15	0.16	0.15	0.15	0.14	0.14	0.31	0.37
Yb	0.98	1.04	0.98	0.99	0.92	0.89	2.19	2.39
Lu	0.15	0.16	0.15	0.16	0.14	0.14	0.36	0.36
Y	10.1	10.8	9.0	9.5	10.6	10.1	22.5	28.0
Zr	181	188	223	195	141	157	266	296
Hf	5.2	5.4	6.7	5.5	4.4	4.9	6.9	8.1
Nb	12	14	14	14	15	15	24	23
Ta	0.89	1.01	0.99	1.06	1.20	1.01	1.06	1.13
Th	25	25	32	27	32	33	18	25
U	3.3	2.9	3.3	4.1	4.2	3.4	2.4	20.9
Pb	17	16	23	21	24	21	26	33
$(La/Yb)_N$	59.15	48.86	43.10	43.09	46.32	98.66	24.36	31.35
δEu	0.73	0.64	0.72	0.71	0.66	0.57	0.64	0.63
Nb/Ta	14.00	13.60	14.01	13.17	12.83	14.52	22.79	20.62

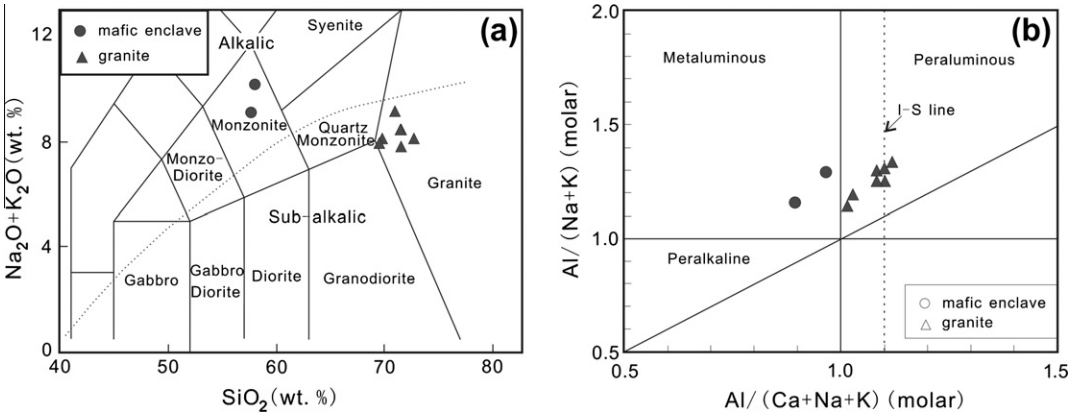

Fig. 5. Classification of the host rock and mafic enclave from the Gushan granite. (a) TAS diagram, with all major element data recalculated to 100% on an H_2O- and CO_2-free basis (after Middlemost (1994)); (b) A/NK [molar ratio $Al_2O_3/(Na_2O + K_2O)$] vs. A/CNK [molar ratio $Al_2O_3/(CaO + Na_2O + K_2O)$] plot.

Nineteen zircons from the Sample 10G07 have initial $^{176}Hf/^{177}Hf$ values between 0.282128 and 0.282196, with an average value of 0.282161. The $\varepsilon_{Hf}(t)$ values range from −17.8 to −20.2, with an average value of −19.0. Seventeen zircons from the Sample 10G11 have initial $^{176}Hf/^{177}Hf$ values between 0.282079 and 0.282227, with an average value of 0.282153. The $\varepsilon_{Hf}(t)$ values are from −16.6 to −22.0, with an average value of −19.3.

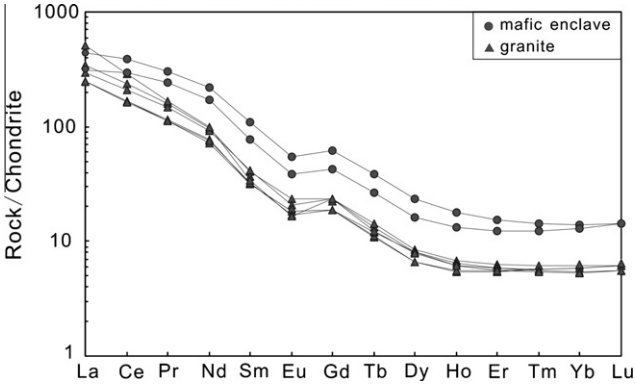

Fig. 6. Chondrite-normalized REE patterns for host granite and the mafic enclaves. The chondrite values used are from Sun and McDonough (1989).

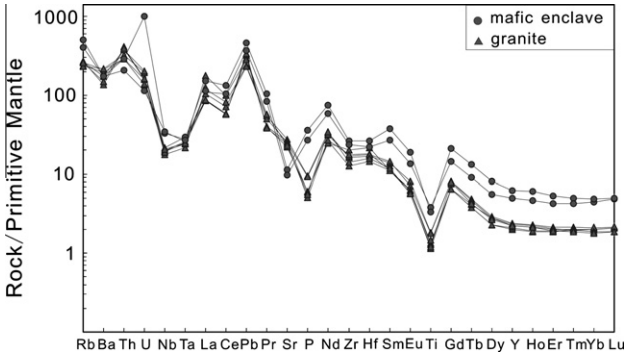

Fig. 7. Primitive mantle (PM) normalized trace element diagrams for host granite and mafic enclaves. The PM values used are from Sun and McDonough (1989).

Zircons from microgranular enclave (Sample 10GS20) show slightly less radiogenic hafnium than the host granodiorite. The initial $^{176}Hf/^{177}Hf$ values range between 0.282142 and 0.282242, with an average value of 0.282186; the $\varepsilon_{Hf}(t)$ values range from −16.1 to −19.6, with an average value of −18.1.

5.5. Sr and Nd isotopic zoning of K-feldspar phenocrysts

Sr isotopic profiles were successfully obtained for five K-feldspar phenocrysts, and Nd isotopic stratigraphies were determined for four phenocrysts (Fig. 10 and Table 5). Although samples for Sr and Nd isotopic analysis involve relatively large spatial resolution within single K-feldspar phenocrysts, they provide a robust indication of the overall trend of Sr and Nd isotopic variations.

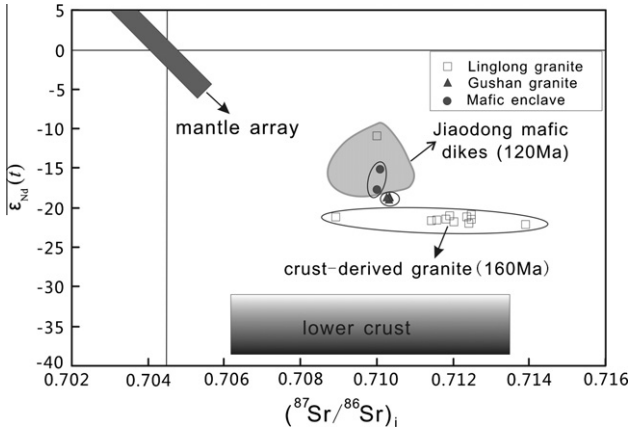

Fig. 8. Sr and Nd isotopic data from the granites and mafic enclaves. The field for lower continental crust (LCC) is from Jahn et al. (1999). Published compositional fields for Early Cretaceous mafic dikes (Yang et al., 2004b; Liu et al., 2009) and the Jurassic crustally-derived Linglong granite (Hou et al., 2007; Zhang et al., 2010) from the Jiaobei terrane are also shown for comparison.

Our data reveal similar core to rim isotopic profiles in all the analyzed K-feldspar phenocrysts. All five grains show systematic increases in initial $^{87}Sr/^{86}Sr$ ratios from core to rim. Grain 10G08-5 displays the largest range in initial $^{87}Sr/^{86}Sr$ ratios: from 0.7101 in the core, 0.7106 in the mantle to 0.7110 in the rim. The other four grains display smaller ranges: with initial $^{87}Sr/^{86}Sr$ ratios of 0.7100–0.7102 in the core, 0.7102–0.7103 in the mantle and 0.7105–0.7108 in the rim. Variation in $\varepsilon_{Nd}(t)$ is generally complementary to initial $^{87}Sr/^{86}Sr$ ratios. Grain 10GS21 and Grain 10GS16 show relatively minor core-to-rim Nd isotopic decrease with $\varepsilon_{Nd}(t)$ of −17.7 to −18.9 in the core and −21.1 to −21.2 in the rim. Grain 10G07 displays large Nd isotopic variation: from −19.2 in the core, −19.5 in the mantle to −27.0 in the rim. Grain 10GS15 illustrates a slightly different Nd isotopic profile, with its core ($\varepsilon_{Nd}(t) = -20.5$) having higher $\varepsilon_{Nd}(t)$ value than the mantle($\varepsilon_{Nd}(t) = -19.6$). However, its rim has low $\varepsilon_{Nd}(t)$ value (−25.7), displaying a general core-to-rim decreasing trend for Nd isotopes similar to the other three grains.

A comparison of the isotopic characteristics of the different K-feldspar phenocrysts shows that the different cores share similar isotopic compositions: initial $^{87}Sr/^{86}Sr$ ratios of cores range between 0.7101 and 0.7102, and $\varepsilon_{Nd}(t)$ range between −17.7 and −20.5. However, different rims display moderate to large ranges in Sr and Nd isotopes: initial $^{87}Sr/^{86}Sr$ ratios and $\varepsilon_{Nd}(t)$ values of rims vary between 0.7105 and 0.7110, and between −21.1 and −27.0 respectively.

Table 3
Sr and Nd isotopic compositions for the Gushan granite and mafic enclaves.

Sample no.	Rb (ppm)	Sr (ppm)	$^{87}Rb/^{86}Sr$	$^{87}Sr/^{86}Sr$	$(^{87}Sr/^{86}Sr)_i$	±2σ	Sm (ppm)	Nd (ppm)	$^{147}Sm/^{144}Nd$	$^{143}Nd/^{144}Nd$	$\varepsilon_{Nd}(t)$	±2σ	T_{DM1}(Ga)	T_{DM2}(Ga)
Granite														
10G09	144.5	520.3	0.8043	0.711652	0.710292	0.000012	4.7	35.9	0.0799	0.511581	−18.9	0.000011	1.79	2.45
10GS20-h	154.5	564.5	0.7922	0.711593	0.710253	0.000011	4.5	31.1	0.0869	0.511596	−18.7	0.000010	1.87	2.44
08G46	167.9	487.6	0.9970	0.711981	0.710295	0.000013	3.8	27.9	0.0834	0.511591	−18.7	0.000011	1.82	2.44
08G47	159.9	477.1	0.9701	0.711939	0.710298	0.000014	4.3	31.7	0.0829	0.511595	−18.6	0.000012	1.81	2.43
Mafic enclave														
10GS20-m	265.2	209.0	3.6760	0.716244	0.710027	0.000011	10.7	71.6	0.0904	0.511647	−17.7	0.000014	1.86	2.36
10GS21	324.8	244.6	3.8478	0.716608	0.710101	0.000011	14.7	91.1	0.0978	0.511785	−15.1	0.000010	1.79	2.15

The initial $^{87}Sr/^{86}Sr$ ratios and $\varepsilon_{Nd}(t)$ values have been calculated at 119 Ma based on the zircon U–Pb dating.
Chondrite Uniform Reservoir (CHUR) values ($^{87}Rb/^{86}Sr = 0.0847$, $^{87}Sr/^{86}Sr = 0.7045$, $^{147}Sm/^{144}Nd = 0.1967$, $^{143}Nd/^{144}Nd = 0.512638$) are used for the calculation. $\lambda_{Rb} = 1.42 \times 10^{-11}$ year^{-1}, $\lambda_{Sm} = 6.54 \times 10^{-12}$ year^{-1} (Lugmair and Harti, 1978).

Table 4
Zircon Hf isotopic compositions for the Gushan granite and mafic enclaves.

Sample no.	t (Ma)	$^{176}Yb/^{177}Hf$	$^{176}Lu/^{177}Hf$	$^{176}Hf/^{177}Hf$	2 s	$\varepsilon_{Hf}(0)$	$\varepsilon_{Hf}(t)$	T_{DM1}(Hf)	T_{DM2}(Hf)	$f_{Lu/Hf}$
Granite (10G07)										
10G07-01	117.7	0.018098	0.000699	0.282175	0.000025	−21.2	−18.7	1510	2361	−0.98
10G07-02	116.1	0.021977	0.000768	0.282145	0.000027	−22.2	−19.8	1554	2429	−0.98
10G07-03	116.7	0.017682	0.000645	0.282146	0.000036	−22.2	−19.7	1548	2426	−0.98
10G07-04	119.3	0.015825	0.000574	0.282131	0.000027	−22.7	−20.2	1566	2458	−0.98
10G07-05	120.8	0.031448	0.001083	0.282152	0.000024	−22.0	−19.4	1558	2412	−0.97
10G07-06	120.4	0.021724	0.000760	0.282132	0.000026	−22.7	−20.1	1573	2456	−0.98
10G07-07	122.3	0.021592	0.000761	0.282176	0.000026	−21.1	−18.5	1511	2356	−0.98
10G07-08	116.6	0.024914	0.000880	0.282169	0.000022	−21.4	−18.9	1526	2376	−0.97
10G07-09	119.8	0.019573	0.000695	0.282188	0.000029	−20.7	−18.2	1493	2332	−0.98
10G07-10	116.4	0.020467	0.000762	0.282161	0.000025	−21.7	−19.2	1533	2394	−0.98
10G07-11	116.7	0.014738	0.000531	0.282155	0.000025	−21.9	−19.4	1531	2406	−0.98
10G07-12	117.3	0.023547	0.000876	0.282200	0.000022	−20.3	−17.8	1482	2306	−0.97
10G07-13	120.0	0.026171	0.000990	0.282198	0.000025	−20.4	−17.8	1490	2311	−0.97
10G07-14	120.4	0.026349	0.000950	0.282178	0.000025	−21.1	−18.5	1517	2355	−0.97
10G07-15	117.6	0.019863	0.000713	0.282164	0.000028	−21.6	−19.0	1526	2385	−0.98
10G07-16	119.5	0.014454	0.000527	0.282176	0.000024	−21.2	−18.6	1502	2358	−0.98
10G07-17	118.7	0.018346	0.000707	0.282158	0.000023	−21.8	−19.2	1534	2398	−0.98
10G07-18	117.6	0.018882	0.000688	0.282171	0.000030	−21.3	−18.8	1515	2370	−0.98
10G07-19	118.7	0.022746	0.000799	0.282161	0.000024	−21.7	−19.2	1534	2393	−0.98
Granite (10G11)										
10G11-01	118.6	0.018172	0.000645	0.282140	0.000025	−22.4	−19.9	1557	2439	−0.98
10G11-02	115.5	0.025404	0.000829	0.282083	0.000029	−24.4	−22.0	1643	2567	−0.98
10G11-03	121.4	0.029151	0.000955	0.282156	0.000027	−21.9	−19.3	1547	2403	−0.97
10G11-04	122.3	0.032677	0.001061	0.282193	0.000027	−20.6	−18.0	1500	2321	−0.97
10G11-05	114.7	0.019640	0.000659	0.282101	0.000029	−23.8	−21.3	1610	2527	−0.98
10G11-06	120.4	0.030008	0.001016	0.282231	0.000027	−19.2	−16.6	1444	2235	−0.97
10G11-07	120.7	0.029381	0.000930	0.282207	0.000044	−20.1	−17.5	1475	2290	−0.97
10G11-08	119.0	0.017390	0.000609	0.282114	0.000033	−23.3	−20.8	1591	2496	−0.98
10G11-09	122.6	0.024220	0.000823	0.282160	0.000029	−21.7	−19.1	1536	2392	−0.98
10G11-10	117.9	0.021130	0.000715	0.282141	0.000030	−22.4	−19.9	1558	2437	−0.98
10G11-11	118.1	0.024211	0.000808	0.282182	0.000030	−20.9	−18.4	1505	2346	−0.98
10G11-12	122.0	0.023666	0.000800	0.282137	0.000026	−22.5	−19.9	1568	2445	−0.98
10G11-13	119.1	0.020409	0.000720	0.282218	0.000029	−19.7	−17.1	1452	2265	−0.98
10G11-14	120.7	0.015580	0.000574	0.282170	0.000022	−21.3	−18.7	1512	2369	−0.98
10G11-15	119.9	0.023602	0.000847	0.282154	0.000029	−21.9	−19.4	1545	2407	−0.97
10G11-16	123.2	0.014857	0.000512	0.282134	0.000024	−22.6	−20.0	1559	2449	−0.98
10G11-17	121.5	0.022497	0.000754	0.282142	0.000025	−22.3	−19.8	1558	2433	−0.98
Mafic enclave (10GS20)										
10GS20-01	116.3	0.019831	0.000674	0.282229	0.000030	−19.3	−16.8	1434	2241	−0.98
10GS20-02	117.9	0.026315	0.000874	0.282156	0.000021	−21.8	−19.3	1543	2404	−0.97
10GS20-03	116.6	0.017043	0.000601	0.282204	0.000028	−20.1	−17.6	1466	2296	−0.98
10GS20-04	120.6	0.020561	0.000738	0.282245	0.000027	−18.7	−16.1	1414	2203	−0.98
10GS20-05	119.8	0.014655	0.000505	0.282155	0.000023	−21.9	−19.3	1529	2403	−0.98
10GS20-06	116.7	0.025589	0.000867	0.282180	0.000022	−21.0	−18.5	1509	2350	−0.97
10GS20-07	116.5	0.017321	0.000590	0.282169	0.000022	−21.4	−18.9	1514	2375	−0.98
10GS20-08	117.6	0.029448	0.000983	0.282182	0.000024	−20.9	−18.4	1512	2347	−0.97
10GS20-09	117.4	0.024273	0.000839	0.282176	0.000025	−21.2	−18.7	1515	2360	−0.97
10GS20-10	120.9	0.023484	0.000799	0.282146	0.000019	−22.2	−19.6	1554	2424	−0.98
10GS20-11	119.3	0.020119	0.000699	0.282180	0.000022	−21.0	−18.5	1504	2350	−0.98
10GS20-12	121.2	0.022613	0.000771	0.282195	0.000022	−20.5	−17.9	1485	2315	−0.98
10GS20-13	122.3	0.017460	0.000593	0.282186	0.000022	−20.8	−18.2	1491	2334	−0.98
10GS20-14	117.9	0.016838	0.000586	0.282183	0.000020	−20.9	−18.4	1495	2344	−0.98
10GS20-15	118.2	0.020981	0.000728	0.282180	0.000022	−21.0	−18.5	1505	2350	−0.98
10GS20-16	116.6	0.014330	0.000487	0.282246	0.000023	−18.7	−16.2	1405	2204	−0.99
10GS20-17	117.8	0.024060	0.000831	0.282211	0.000025	−19.9	−17.4	1466	2282	−0.97

The following parameters were applied to calculation: $(^{176}Lu/^{177}Hf)_{CHUR} = 0.0332$, $(^{176}Hf/^{177}Hf)_{CHUR,0} = 0.282772$, $(^{176}Lu/^{177}Hf)_{DM} = 0.0384$, $(^{176}Hf/^{177}Hf)_{DM,0} = 0.28325$ (Blichert-Toft and Albaréde, 1997; Griffin et al., 2000), ^{176}Lu decay constant $\lambda = 1.867 \times 10^{-11}$ a^{-1} (Söderlund et al., 2004).

6. Discussion

6.1. Mafic–felsic magma interaction process in the late magmatic history

6.1.1. Origin of MMEs

Most researchers now agree that MMEs are formed by magma mixing or mingling processes, which are characteristics of many calc-alkaline felsic intrusions. The enclaves from the Gushan granite have the same age but distinctive isotopic features from the host granite. In addition, they display fine-grained igneous textures and contain acicular apatite. These features are similar to those MMEs reported elsewhere (Vernon, 1984; Didier and Barbarin, 1991; Waight et al., 2000, 2001; Yang et al., 2004a; Kumar and Rino, 2006; Chen et al., 2009a) and have been attributed to rapid cooling, resulting from the injection of small volumes of hotter mafic magma into cooler felsic melts. The presence of K-feldspar xenocrysts in the MMEs indicates that the mixing event represented by the MMEs occurred mainly after crystallization of K-feldspar which is one of the last minerals to become saturated in felsic magmas (Piwinskii, 1968; Whitney, 1975; Means and Park, 1994). Therefore, the enclaves in the Gushan granite are considered

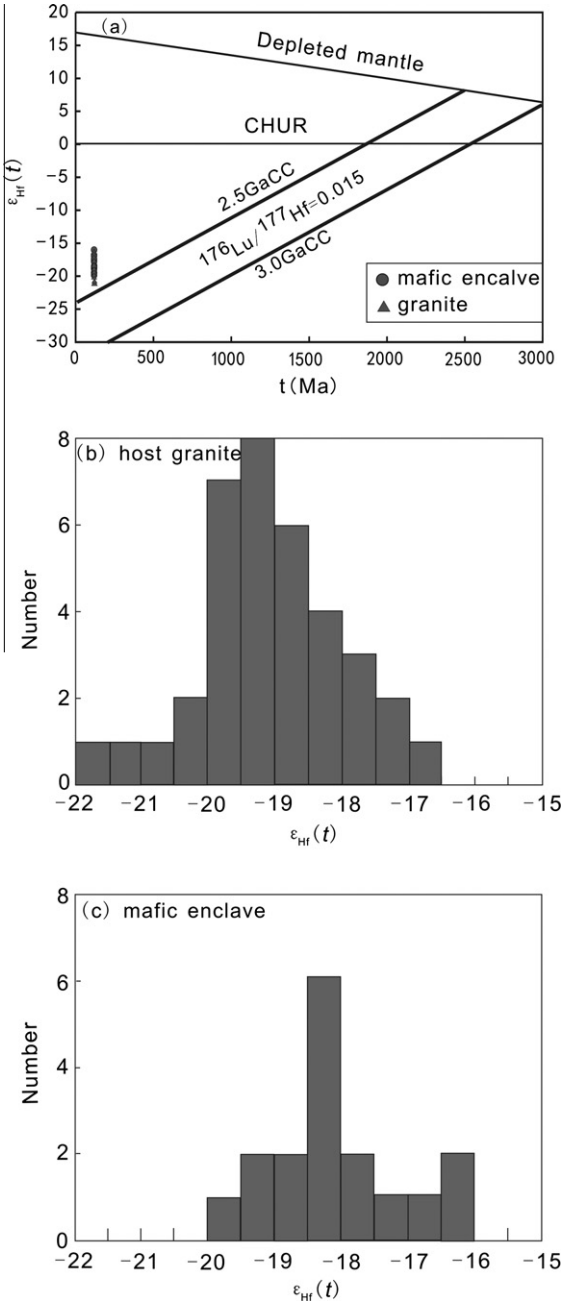

Fig. 9. Diagram of Hf isotopic evolution in zircons (a) and frequency histogram of $\varepsilon_{Hf}(t)$ for the granite (b) and mafic enclaves (c). CHUR, chondritic uniform reservoir; CC, continental crust. Depleted mantle evolution is calculated by using $\varepsilon_{Hf}(t) = 16.9$ at $t = 0$ Ma and $\varepsilon_{Hf}(t) = 6.4$ at $t = 3.0$ Ga, the applied parameters as in Table 4. The corresponding lines of crustal extraction are calculated using the $^{176}Lu/^{177}$ Hf ratio of 0.015 for the average continental crust (Griffin et al., 2002).

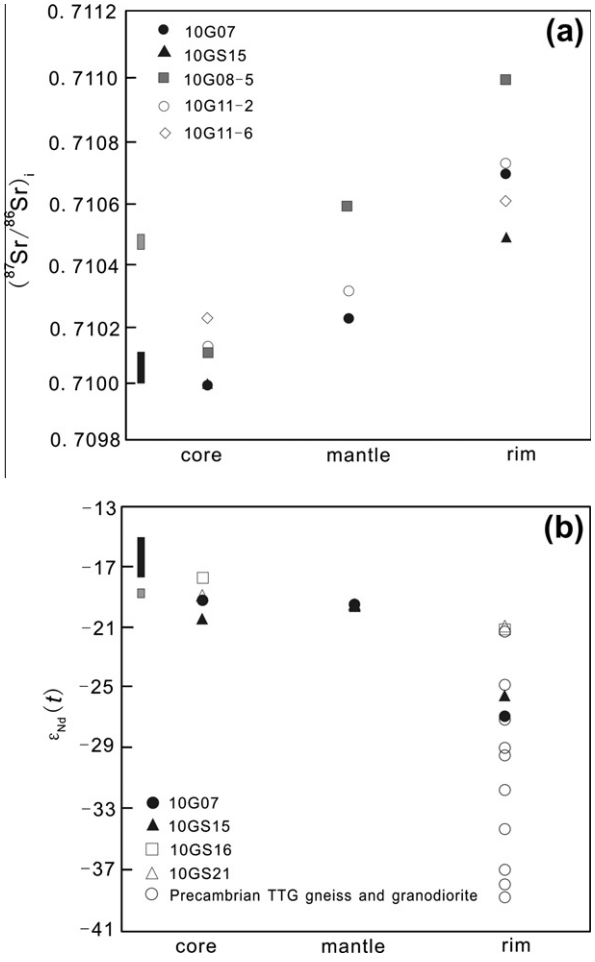

Fig. 10. (a) Variations in Sr isotope within five K-feldspars. (b) Variations in Nd isotopic compositions within four K-feldspars. The Nd isotopic data of Precambrian TTG gneiss and granodiorite is from Jahn et al. (2008). Gray boxes represent Sr and Nd isotopic composition of host granite; Black boxes represent Sr and Nd isotopic composition of MMEs.

to be formed through mafic–felsic magma interaction in the generation of the host granite in the relatively late magmatic history.

In the course of magma interaction, both chemical and isotopic compositions tend to reach homogenization, but radiogenic isotopic equilibrium is attained more rapidly than chemical equilibrium (Lesher, 1990, 1994). MMEs and the host granite have similar Sr isotopes, whereas there are moderate Nd isotopic discrepancies between them (Fig. 8). This should arise from different diffusion rates of Sr and Nd in melts (Cherniak, 2003). Interestingly, there is a broad overlap in Hf isotopic compositions between zircons from the enclave and host granite. Zircons are normally expected to be a relatively early crystallizing phase, and then should perhaps predate most diffusive equilibrium between the mafic magma and host granite. Thus, they can preserve the greatest possible contrast in isotopic compositions: zircons in the host granite may have crystallized prior to major influxes of mafic magma and therefore should have the most crustal composition, whereas zircons in the mafic enclave should preserve the compositions of the mafic melts. However, this does not appear to be the case in this study. As noted above, apatites have the acicular habit, which is suggestive of its early-stage rapid cooling and crystallization. Zircons do not have the needle shape and most of them contain needle apatite inclusions. These features indicate that zircons in MMEs were not the very early crystallizing phase. On the other hand, if the enclave is related to an original mafic magma, zircons were probably not a stable phase. It was only after considerable chemical equilibration had taken place that silica and zirconium contents would be high enough to allow for zircon crystallization. This is consistent with the similar Hf isotopic compositions of zircon from both enclave and granite.

6.1.2. Possible magma sources

As mentioned above, enlaves within the Gushan Granite are products of mafic–felsic magma interactions. What is the possible source for the mafic magma end-members? Elements and isotopes tend to reach equilibrium during magma mixing process, so the

Table 5
Sr and Nd isotopic compositions for K-feldspars.

Sample no.	Rb (ppm)	Sr (ppm)	$^{87}Rb/^{86}Sr$	$^{87}Sr/^{86}Sr$	$\pm2\sigma$	$^{87}Sr/^{86}Sr(i)$	Sm (ppm)	Nd (ppm)	$^{147}Sm/^{144}Nd$	$^{143}Nd/^{144}Nd$	$\pm2\sigma$	$\varepsilon(0)$	$\varepsilon(t)$
10GS15c	141.1	1999.9	0.2041	0.710293	0.000010	0.709948	0.03	0.46	0.0435	0.511470	0.000011	−22.8	−20.5
10GS15m							0.04	0.43	0.0551	0.511526	0.000005	−21.7	−19.6
10GS15r	330.9	538.4	1.7794	0.713467	0.000009	0.710458	0.06	0.43	0.0849	0.511235	0.000011	−27.4	−25.7
10G07c	139.8	1945.4	0.2079	0.710340	0.000009	0.709988	0.03	0.42	0.0450	0.511535	0.000011	−21.5	−19.2
10G07m	177.0	1137.4	0.4504	0.710988	0.000040	0.710226	0.02	0.19	0.0657	0.511536	0.000008	−21.5	−19.5
10G07r	341.7	687.3	1.4393	0.713193	0.000008	0.710759	0.02	0.17	0.0718	0.511156	0.000009	−28.9	−27.0
10G08-5c	131.6	1441.2	0.2643	0.710558	0.000040	0.710111							
10G08-5m	198.7	777.4	0.7397	0.711841	0.000020	0.710590							
10G08-5r	241.5	456.1	1.5328	0.713580	0.000040	0.710987							
10G11-2c	102.5	1820.4	0.1630	0.710418	0.000030	0.710143							
10G11-2m	192.1	1033.8	0.5378	0.711235	0.000030	0.710326							
10G11-2r	214.6	595.9	1.0424	0.712491	0.000030	0.710728							
10G11-6c	112.3	1400.8	0.2321	0.710625	0.000040	0.710232							
10G11-6r	225.5	625.8	1.0432	0.712375	0.000030	0.710610							
10GS21c							0.03	0.42	0.0372	0.511545	0.000011	−21.3	−18.9
10GS21m							0.03	0.29	0.0674	0.511529	0.000010	−21.6	−19.7
10GS21r							0.03	0.25	0.0778	0.511465	0.000010	−22.9	−21.1
10GS16c							0.03	0.43	0.0434	0.511611	0.000009	−20.0	−17.7
10GS16r							0.05	0.35	0.0827	0.511462	0.000013	−22.9	−21.2

Initial $^{87}Sr/^{86}Sr$ ratios and $\varepsilon_{Nd}(t)$ value were calculated using an age of 119 Ma.
Chondrite Uniform Reservoir (CHUR) values ($^{87}Rb/^{86}Sr = 0.0847$, $^{87}Sr/^{86}Sr = 0.7045$, $^{147}Sm/^{144}Nd = 0.1967$, $^{143}Nd/^{144}Nd = 0.512638$) are used for the calculation. $\lambda_{Rb} = 1.42 \times 10^{-11}$ year^{-1}, $\lambda_{Sm} = 6.54 \times 10^{-12}$ year^{-1} (Lugmair and Harti, 1978).
c – core; m – mantle; r – rim.

parental mafic melts should have lower SiO_2 (<57 wt.%), higher MgO($Mg^{\#} > 56$), Ni(>41 ppm) and Co(>18 ppm) concentrations, more radiogenic Nd isotopic ratios ($\varepsilon_{Nd}(t) > -15.1$) and less radiogenic $^{87}Sr/^{86}Sr$ ratios (<0.710) than those displayed either by the granite or by the mafic enclaves. These compositional features can be explained either as melts derived from an enriched lithospheric mantle or those from depleted (asthenospheric) mantle but with incorporation of crustal material. A simple mixing model (based on Langmuir et al., 1978) based on Sr and Nd isotopes (the depleted mantle is from Zindler et al. (1984) with Sr = 190 ppm, $I_{Sr} = 0.703$, Nd = 19 ppm, $\varepsilon_{Nd} = +9$; the middle to lower continental crust beneath the eastern NCC is from Jahn et al. (1999), with Sr = 300 ppm, $I_{Sr} = 0.710$, Nd = 24 ppm, $\varepsilon_{Nd} = -30$) show that enclaves were unlikely to derive from depleted mantle, followed by contamination of crustal materials, because it would require assimilation of 60% crustal components. Such a voluminous assimilation would severely modify the major element composition of the magmas. In fact, former works demonstrate that the lithospheric mantle beneath eastern NCC was isotopically enriched during the Early Cretaceous (Zhang et al., 2002; Xu et al., 2004; Yang et al., 2004b; Liu et al., 2009). In the Jiaodong Peninsula, the earliest asthenosphere derived magmas are identified to be of ca. 73–82 Ma in the Mesozoic (Yan et al., 2003; Zhang et al., 2003, 2008). In addition, widespread mafic dikes of ~120 Ma have been identified in the Jiaobei terrane, and are believed to originate from an enriched lithospheric mantle (Yang et al., 2004b; Liu et al., 2009). Therefore, we deduce that parental magmas of the mafic enclaves were derived from an enriched lithospheric mantle source but experienced moderate chemical and isotopic exchange with host granitic magma. Furthermore, the significant depletion in Sr in spider diagram as well as the moderate negative Eu anomalies of the mafic enclaves indicates that plagioclase may have been fractionated during the evolution of the mafic magma.

The host granites have high SiO_2 (69.48–72.72 wt.%), $K_2O + Na_2O$ (7.83–9.15 wt.%) and low MgO (0.70–1.07 wt.%) contents, high initial $^{87}Sr/^{86}Sr$ ratios of 0.7103–0.7104, strongly negative $\varepsilon_{Nd}(t)$ (−18.6 to −18.9) and zircon $\varepsilon_{Hf}(t)$ (−16.6 to −22.0) values. In addition, they are enriched in HREE and LILE but depleted in HFSE, and have Nb/Ta ratio of 12.8–14.5 which is close to that of the average continental crust (11–13, Green, 1995; Barth et al., 2000). These are mainly the characteristics of crustal melts. The host granite also possesses high initial $^{87}Sr/^{86}Sr$ ratios (0.7103–0.7104) but low Rb/Sr ratios (0.26–0.37), indicating that the rock was derived from a source with a long residence time. This is also indicated by the older whole-rock Nd model ages (Table 3), which are similar to the crustal ages of the eastern NCC (Wu et al., 2005b; Jahn et al., 2008). Thus, the ancient NCC lower crust is the probable candidate for the main source of the Gushan granite.

However, it should be noted that $\varepsilon_{Nd}(t)$ values of the Gushan granite are relatively higher than published lower crustal values for the North China Craton and those of Jurassic crustally-derived granite in the Jiaobei terrane (Fig. 8). In addition, the Hf isotopic compositions of the Gushan granite fall above the 2.5 Ga continental crust evolutional line (Fig. 9a). These features can be explained if they were mainly derived from partial melting of an ancient crustal source coupled with addition of small amounts of mantle-derived magmas. This is consistent with the presence of small portion of MMEs.

6.2. Continuous contamination process

6.2.1. Equilibration possibilities of Sr–Nd isotopes in K-feldspar

As noted in a previous section, the K-feldspar within the Gushan granite preserve evidence for sub-solidus deuteric alteration, a process that would also produce intracrystalline isotopic heterogeneities (Siebel et al., 2005). However the complimentary nature of Sr and Nd isotopic variations indicate that our data are robust and reflect primary igneous characteristics rather than interaction with deuteric fluids for the following reasons:

(1) If the systematic core-to-rim Sr–Nd isotopic heterogeneity was caused by deuteric alteration, the distribution of the altered domains should be regular and/or alteration intensity should change systematically from core to rim. However, neither obvious regular distribution of turbid and non-turbid materials within sections nor a systematic pattern of alteration intensity from core to rim exists in our samples (Fig. 3b).

(2) Sr isotope diffusion in feldspar (plagioclase and K-feldspar) occurs more rapidly under hydrous conditions (Cherniak and Watson, 1992, 1994; Giletti, 1991; Giletti and Casserly, 1994), and therefore, pervasive fluid flow could effectively reset the sensitive Rb–Sr system, producing homogeneous isotope signatures. However, large Sr isotopic heterogeneities are observed both within single crystals and between rims of different crystals. Variable or spatially limited deuteric alteration may result in irregular isotopic patterns in certain crystals; however our results show complementary divergent trends of Sr and Nd isotopes in all the analyzed crystals. Thus, regardless of the mechanisms and intensities of deuteric alteration, it would be difficult for any one fluid to cause the observed Sr–Nd isotopic profiles.
(3) Nd diffusion may be several orders of magnitude slower than Sr diffusion in feldspars, and previous works have shown that the Sm–Nd isotope system is very resilient to hydrothermal alteration (Michard, 1989; Cherniak, 2003). As mentioned above, a small portion of plagioclase crystals were altered and the biotite and hornblende remain fresh, which exclude the possibility of any intense alteration. It is hard to imagine that a slight to moderate alteration process would produce such a profound effect on the robust Nd isotope ($\varepsilon_{Nd}(t)$ values range from −17.7 to −27.0).
(4) If the isotopic heterogeneities in K-feldspars were really caused by a fluid, the fluid should have an isotopic composition of $^{87}Sr/^{86}Sr > 0.7110$ and $^{143}Nd/^{144}Nd < 0.5111$, considering the isotopic compositions of the host granite. However, no trace of such fluids has been observed in the Jiaobei terrane so far.

Therefore, despite a protracted cooling and deuteric alteration history, we consider that the Sr–Nd isotopic profiles reflect primary changes in the host magma composition during crystallization.

6.2.2. Continuous contamination

The increase in initial $^{87}Sr/^{86}Sr$ ratios from the cores to outer domains of the K-feldspar grains is consistent with assimilation of an isotopically more evolved melt. Likewise, similar Sr isotope trends in feldspar phenocrysts have been interpreted in terms of a magma chamber undergoing crustal contamination (Cox et al., 1996; Tepley and Davidson, 2003; Font et al., 2008). In almost all the analyzed crystals (Grain 10GS15 shows a slightly different Nd-isotope profile), the $\varepsilon_{Nd}(t)$ values decrease from core to rim and are complementary to initial $^{87}Sr/^{86}Sr$ ratios, which is also in accord with the contamination model—with K-feldspar phenocryst cores crystallizing in isotopically "more-mantle like" magma whereas the rims formed from an isotopically "more crustal-like" magma. The progressive increases in initial Sr isotope and decreases in $\varepsilon_{Nd}(t)$ in the phenocrysts argue that contamination processes were likely to have occurred throughout the K-feldspar crystallization history. However, the marked changes in Sr and Nd isotopes are only observed within rims of the phenocrysts, which might be due to the relatively low volume of the remaining host magma as compared to the incoming contaminated magma, or might even record the input of an isotopically more evolved magma (Fig. 11b and c). Notably, crustally-derived enclaves are absent in the host granite. It is probable that all crustal felsic components entrained in the magma were easily melted because of their low melting point or the presence of fluids which can lower the melting temperature. Thus, the signatures of crustal components are preserved only in the isotopic chemistry of the zoned K-feldspar phenocrysts.

Because of its slow equilibration rate during magma mixing, Nd isotope can be effectively used to trace primary magma sources. The $\varepsilon_{Nd}(t)$ of K-feldspar rims ranges between −21.1 and −27.0, but only crystals with relatively low $\varepsilon_{Nd}(t)$ (−25.7 to −27.0) values respond to the contamination process sensitively. Since isotopic exchange occurred in the course of contamination, the contaminated material should have $\varepsilon_{Nd}(t)$ lower than −27.0 when compared with the isotopic compositions of the host granite. This significantly Nd isotope enriched feature is comparable with those of Precambrian TTG gneisses and granodiorites in the upper crust in the studied area (Jahn et al., 2008). Therefore, we argue here that low $^{143}Nd/^{144}Nd$ upper crustal materials, such as Precambrian basement rocks, were the main crustal components incorporated by the magma.

Even though all the analyzed samples display similar and systematic Sr and Nd isotopic variations, moderate to large Sr and Nd isotopic contrast is shown by different K-feldspar rims. K-feldspar rims grow in the relatively late stage of cooling history, during which magma becomes cooler, more viscous and very crystal rich. In this case, isotopic exchange, especially the Nd isotopic exchange, may be retarded in an opening magma chamber and therefore, the magma body is isotopically heterogeneous. Individual crystals would have recorded the changing isotopic compositions in their local part of the chamber. For instance, crystals growing at the close proximity of the wall-rocks may record, in a more pronounced level, the effects of crustal contamination during their growth, particularly where there is a sharp isotopic gradient between an intruding melt and the wall rocks. Crystal growth in the interior of the magma body, away from the prominent effects of contamination, will be characterized by less isotopic heterogeneities (Fig. 11c). Similar scenarios have been observed in several former studies (Knesel et al., 1999; Halama et al., 2002; Tepley and Davidson, 2003).

6.3. Comparison between intracrystalline and whole-rock isotopic analysis

The average Sr isotopic compositions of K-feldspar are similar to those of whole rocks, whereas most $\varepsilon_{Nd}(t)$ values from K-feldspar are lower than those of whole rocks (Fig. 10). K-feldspar is one of the major minerals composing the granite and Sr is compatible in it, so it dominates the Sr budget of the whole rock. However, K-feldspars only represent a small portion of the Nd budget in the whole rock due to low concentration of Nd in it. The relatively early crystallized phases, such as hornblende, zircon, and apatite, represent a significant portion of the whole rock Nd budget and are expected to have higher $\varepsilon_{Nd}(t)$ values. This is also supportive of the assimilation of isotopically more evolved magma during the K-feldspar crystallization history.

It is also remarked that the range in isotopic compositions in the K-feldspars ($^{87}Sr/^{86}Sr$ from 0.7099 to 0.7110; $\varepsilon_{Nd}(t)$ from −17.7 to −27.0) is considerably larger than isotopic ranges of the whole rocks($^{87}Sr/^{86}Sr$ is 0.7103; $\varepsilon_{Nd}(t)$ from −18.6 to −18.9) (Fig. 10). These results indicate that the complex magmatic histories observed in isotopically zoned phenocrysts in modern volcanic rocks can also be preserved in minerals from much older, slower cooled plutonic rocks. What is more, abundant isotopic heterogeneity may be averaged in the whole rock analyses, so great care must be taken in carrying whole rock isotopic analyses in plutonic rocks that show field evidence for magma mixing/mingling.

6.4. Multiple magma pulses

Based on petrography, geochemistry and isotope studies, we infer a complex, multi-stage magma process for the formation of the Gushan granite. The granite with high initial $^{87}Sr/^{86}Sr$ ratios and highly negative $\varepsilon_{Nd}(t)$ and zircon $\varepsilon_{Hf}(t)$ values was mainly derived from partial melting of ancient lower crust, and was mixed with

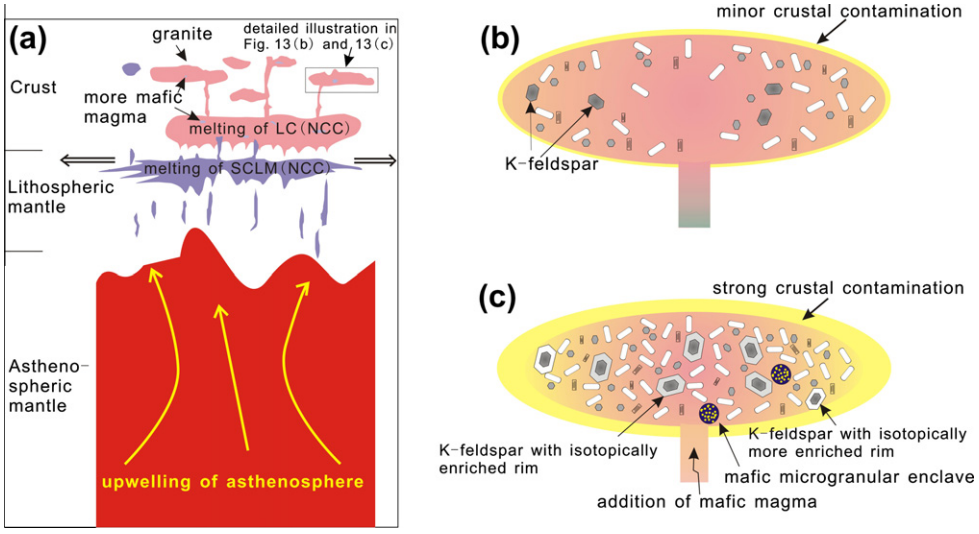

Fig. 11. Cartoons illustrating the suggested geodynamic model and magma evolution for the Gushan granite. (a) Upwelling of asthenosphere as well as lithospheric extension, leading to partial melting of the enriched lithospheric mantle and subsequent dehydration melting of ancient lower crust coupled with mantle–crust interactions; (b) relatively slight wall-rock contamination in the earlier cooling history, during which K-feldspar core and mantle crystallized; (c) in the later cooling history, the effect of contamination was more significant maybe due to the lower volume of host melt. K-feldspar crystals closer to the wall-rock recorded more enriched isotopic characteristics, whereas those growing in the inner part of chamber recorded less enriched isotopic features. Globules of more mafic melt are injected in the host magma in the late stage and are now represented in modified form by mafic microgranular enclaves. NCC – North China Craton; SCLM – subcontinental lithospheric mantle; LC – lower crust.

minor amount of fractionated enriched lithospheric mantle-derived magmas in the late cooling history. Meanwhile, the ascent and crystallization of the host magma occurred along with progressive incorporation of the upper crustal materials.

In previous studies (Waight et al., 2000; Gagnevin et al., 2005), Sr–Nd or Sr isotopic profiles of feldspar phenocrysts have been shown to be consistent with the existence of mafic enclaves, indicating influx of more mafic and isotopically more mantle-like magma. However, in spite of the existence of mafic enclaves, the Sr–Nd isotopic zoning of K-feldspar in the Gushan granite primarily reflects assimilation of more evolved crustal material rather than the addition of more primitive melts. One explanation is that during the stage of K-feldspar crystallization, assimilation of upper crustal material produced more significant effects on the isotopic compositions of host magma as compared with mafic–felsic magma interaction. A large isotopic contrast exists between the host granite and Precambrian basement rocks (Fig. 10b), and therefore the addition of a small volume of upper crustal material would drastically change the isotopic composition, and eclipse the injection of enriched lithospheric mantle-derived mafic magma. A more compelling possibility is that the addition of more mafic magma now recorded as MMEs occurred mainly after the crystallization of K-feldspar. As noted above, K-feldspar phenocrysts which resemble crystals from the host granite are commonly found in the MMEs. It has been largely accepted that such crystals were transferred from the host magma into a mingled mafic melt, most probably while the enclave magma was in the semi-plastic state (Barbarin, 1990; Waight et al., 2000). Therefore, in such a scenario the changing magma compositions in the alkali feldspars represent processes occurring prior to magma mixing to produce the MME and crystal transfer.

6.5. Geodynamic setting for the formation of the Gushan granite

In the Jiaobei terrane, the Gushan granite is coeval with the eruption of bimodal volcanic rocks (Fan et al., 2001), the large scale gold mineralization (Wang et al., 1998; Fan et al., 2005), the formation of metamorphic core complexes (Davis et al., 2001; Darby et al., 2004; Liu et al., 2005) and pull-apart basins (Meng, 2003; Menzies et al., 2007). In general, the tectonic setting of the eastern NCC during the Early Cretaceous was lithospheric thinning and extension perhaps resulting from subduction of the Paleo-Pacific plate (Wu et al., 2005a; Xu, 2007).

We propose the following geodynamic model (Fig. 11a) for the generation of the Gushan granite. During the Early Cretaceous, asthenospheric upwelling and an extensional tectonic setting, probably related to the roll back or change of the subduction direction of Pacific plate (Sun et al., 2007; Xu et al., 2009; Goss et al., 2010), led to elevated geotherms, resulting in the partial melting of the previously enriched lithospheric mantle and underplating of mafic magma below the eastern NCC. Underplating of mantle-derived, hot mafic magmas into a continental crust provided the heat source to induce dehydration melting of the lower crust and subsequent production of granitic melt. The upward migrating felsic magma at relatively high temperatures heated up the wall-rocks in the upper crust, allowing for incorporation of the crustal components. Continued cooling and decrease in the volume of host granitic melt made the effects of contamination more prominent towards the later stages (Fig. 11b and c). In the late stage, the injection of pulses of mafic magma into a felsic magma chamber led to the formation of mafic enclaves (Fig. 11c). We thus propose that the Gushan granite is a product of lithospheric thinning that led to extensive underplating of mantle-derived magma and subsequent partial melting of the lower crust, and preserves the signature of magma interaction and continuous contamination in a largely extensional tectonic setting.

7. Conclusions

The Gushan granite was emplaced in the Early Cretaceous (~120 Ma). It was dominantly derived by partial melting of ancient lower crustal sources within a geodynamic setting of lithospheric thinning and regional extension. MMEs within the host granite indicate that small-scale mafic magma was involved in the granitic magma chamber in the late cooling history and mafic–felsic magma interaction had happened. Available data suggest that the

mafic magma was partial melts of enriched lithospheric mantle and its evolved products.

Our results have also revealed notable primary isotopic heterogeneity within large K-feldspar crystals on a millimeter scale in the Gushan granite in spite of the long cooling history and sub-solidus alteration. Isotopic profiles across K-feldspar phenocryst are consistent with a continuous contamination process, with the Precambrian basements rocks in the region serving as potential contaminants. The isotopic heterogeneity between different K-feldspar crystals might have resulted from their crystallization in different domains within the magma chamber, with crystals which have more evolved isotopic characters growing closer to the wall rock. Our results indicate that the original isotopic disparities in minerals within old, slower cooled plutonic rocks can persist for extended time periods, and can be effectively used to decipher magmatic history.

Acknowledgements

We are grateful to Dr. Tod Waight for thoughtful comments on the original manuscript, to Drs. Qing Qian, Fu-Kun Chen, and Jing-Hui Guo for the fruitful discussions. Professor Franco Pirajno, an anonymous reviewer and the Editor-in-Chief Prof. Bor-ming Jahn are thanked for their constructive and valuable comments which greatly contributed to the improvement of the manuscript. We also thank Ping Xiao, Zhu-yin Chu and Qian-Nan Li for assistance with isotope work, Wen-Jun Li for help with the trace element analysis, Hong-Wei Fang and Ling-Min Zhang for help with zircon separation and CL imaging, and Zhao-Chu Hu for help during zircon LA-ICPMS U–Pb dating. This study was financially supported by the Natural Science Foundation of China (41173056) and the Crisis Mines Continued Resources Exploration Project of China Geological Survey (20089930).

References

Alves, A., Janasi, V.A., Simonetti, A., Heaman, L., 2009. Microgranitic enclaves as products of self-mixing events: a study of open-system processes in the Mauá Granite, São Paulo, Brazil, based on *in situ* isotopic and trace elements in plagioclase. Journal of Petrology 50, 2221–2247.

Barbarin, B., 1990. Plagioclase xenocrysts and mafic magmatic enclaves in some granitoids of the Sierra Nevada batholith, California. Journal of Geophysical Research 95, 17747–17756.

Barth, M.G., McDonough, W.F., Rudnick, R.L., 2000. Tracking the budget of Nb and Ta in the continental crust. Chemical Geology 165, 197–213.

Blichert-Toft, J., Albaréde, F., 1997. The Lu–Hf isotope geochemistry of chondrites and the evolution of the mantle–crust system. Earth and Planetary Science Letters 148, 243–258.

Chadwick, J.P., Troll, V.R., Ginibre, C., Morgan, D., Gertisser, R., Waight, T.E., Davison, J.P., 2007. Carbonate assimilation at Merapi Volcano, Java, Indonesia: insights from crystal isotope stratigraphy. Journal of Petrology 48, 1793–1812.

Chen, B., Chen, Z.C., Jahn, B.M., 2009a. Origin of mafic enclaves from the Taihang Mesozoic orogen, north China craton. Lithos 110, 343–358.

Chen, B., He, J.B., Ma, X.H., 2009b. Petrogenesis of mafic enclaves from the north Taihang Yanshanian intermediate to felsic plutons: evidence from petrological, geochemical, and zircon Hf–O isotopic data. Science in China (D) 52, 1331–1344.

Cherniak, D.J., 2003. REE diffusion in feldspar. Chemical Geology 193, 25–41.

Cherniak, D.J., Watson, E.B., 1992. A study of strontium diffusion in K-feldspar, Na–K feldspar and anorthite using Rutherford backscattering spectroscopy. Earth and Planetary Science Letters 113, 411–425.

Cherniak, D.J., Watson, E.B., 1994. A study of strontium diffusion in plagioclase using Rutherford backscattering spectroscopy. Geochimica et Cosmochimica Acta 58, 5179–5190.

Chu, Z.Y., Wu, F.Y., Walker, R.J., Rudnick, R.L., Pitcher, L., Puchtel, I.S., Yang, Y.H., Wilde, S.A., 2009a. Temporal evolution of the lithospheric mantle beneath the eastern North China Craton. Journal of Petrology 50, 1857–1898.

Chu, Z.Y., Chen, F.K., Yang, Y.H., Guo, J.H., 2009b. Precise determination of Sm, Nd concentrations and Nd isotopic compositions at the nanogram level in geological samples by thermal ionization mass spectrometry. Journal of Analytical Atomic Spectrometry 24, 1534–1544.

Cox, R.A., Dempster, T.J., Bell, B.R., Rogers, G., 1996. Crystallisation of the Shap Granite: evidence from zoned K-feldspar megacrysts. Journal of the Geological Society, London 153, 625–635.

Darby, B.J., Davis, G.A., Zhang, X.H., Wu, F.Y., Wilde, S.A., Yang, J.H., 2004. The newly discovered Waziyu metamorphic core complex, YiwuluShan, western Liaoning Province, northwest China. Earth Science Frontiers 11, 145–155.

Davidson, J.P., Tepley III, F.J., 1997. Recharge in volcanic systems: evidence from isotopic profiles of phenocysts. Science 275, 826–829.

Davidson, J.P., Tepley, F.J., Knesel, K.M., 1998. Isotopic fingerprinting may provide insights into evolution of magmatic systems. EOS, Transactions American Geophysical Union 79, 185, 189, 193.

Davidson, J.P., Tepley III, F.J., Palacz, Z., Meffan-Main, S., 2001. Magma recharge, contamination and residence times revealed by *in situ* laser ablation isotopic analysis of feldspar in volcanic rocks. Earth and Planetary Science Letters 184, 427–442.

Davidson, J.P., Charlier, B.L.A., Hora, J.M., Perlroth, R., 2005. Mineral isochrons and isotopic fingerprinting: pitfalls and promises. Geology 33, 29–32.

Davidson, J.P., Morgan, D., Charlier, B.L.A., Harlou, R., Hora, J.M., 2007. Microsampling and isotopic analysis of igneous rocks: implications for the study of magmatic systems. Annual Review of Earth and Planetary Science 35, 273–311.

Davidson, J.P., Font, L., Charlier, L.A., Tepley, F.J.I.I.I., 2008. Mineral-scale Sr isotope variation in plutonic rocks – a tool for unravelling the evolution of magma systems. Transactions of the Royal Society of Edinburgh: Earth Sciences 97, 357–367.

Davis, G.A., Zheng, Y.D., Wang, C., Darby, B.J., Zhang, C.H., Gehrels, G., 2001. Mesozoic tectonic evolution of the Yanshan fold and thrust belt, with emphasis on Hebei and Liaoning Provinces northern China. Geological Society of America Memoirs 194, 171–197.

Didier, D., Barbarin, B., 1991. Enclaves and Granite Petrology, Developments in Petrology. Elsevier Science Publications, Amsterdam, pp. 1–625.

Eichelberger, J.C., 1975. Origin of andesite and dacite: evidence of mixing at Glass Mountain in California and other circum Pacific volcanoes. Geological Society of America Bulletin 86, 1381–1391.

Eichelberger, J.C., 1980. Vesiculation of mafic magma during replenishment of silicic magma reservoirs. Nature 288, 446–450.

Fan, W.M., Guo, F., Wang, Y.J., Lin, G., Zhang, M., 2001. Post-orogenic bimodal volcanism along the Sulu Orogenic Belt in Eastern China. Physics and Chemistry of the Earth Part A: Solid Earth and Geodesy 26, 733–746.

Fan, H.R., Hu, F.F., Yang, J.H., Shen, K., Zhai, M.G., 2005. Fluid evolution and large-scale gold metallogeny during Mesozoic tectonic transition in the eastern Shandong province. Acta Petrologica Sinica 21, 1317–1328.

Font, L., Davison, J.P., Pearson, D.G., Nowell, G.M., Jerram, D.A., Ottley, C.J., 2008. Sr and Pb isotope micro-analysis of plagioclase crystals from skye lavas: an insight into open-system processes in a flood basalt province. Journal of Petrology 49, 1449–1471.

Gagnevin, D., Daly, J.S., Poli, G., Morgan, D., 2005. Microchemical and Sr isotopic investigation of zoned K-feldspar megacrysts: insights into the petrogenesis of a plutonic system and disequilibrium processes during crystal growth. Journal of Petrology 46, 1689–1724.

Geng, Y., Du, L., Ren, L., 2012. Growth and reworking of the early Precambrian continental crust in the North China Craton: Constraints from zircon Hf isotopes. Gondwana Research 21, 517–529.

Giletti, B.J., 1991. Rb and Sr diffusion in alkali feldspars, with implications for cooling histories of rocks. Geochimica et Cosmochimica Acta 55, 1331–1343.

Giletti, B.J., Casserly, J.E.D., 1994. Strontium diffusion kinetics in plagioclase feldspars. Geochimica et Cosmochimica Acta 58, 3785–3793.

Goolaerts, A., Mattielli, N., Jong, J.D., Weis, D., Scoatea, J.S., 2004. Hf and Lu isotopic reference values for the zircon standard 91500 by MC–ICP-MS. Chemical Geology 206, 1–9.

Goss, S.C., Wilde, S.A., Wu, F.Y., Yang, J.H., 2010. The age, isotopic signature and significance of the youngest Mesozoic granitoids in the Jiaodong Terrane, Shandong Province, North China Craton. Lithos 120, 309–326.

Green, T.H., 1995. Significance of Nb/Ta as an indicator of geochemical processes in the crust–mantle system. Chemical Geology 120, 347–359.

Griffin, W.L., Pearson, N.J., Belousova, E., Jackson, S.E., Achterbergh, E.V., O'Reilly, S.Y., Shee, S.R., 2000. The Hf isotope composition of cratonic mantle: LAM-MC-ICPMS analysis of zircon megacrysts in kimberlites. Geochimica et Cosmochimica Acta 64, 133–147.

Griffin, W.L., Wang, X., Jackson, S.E., Pearson, N.J., O'Reilly, S.Y., Xu, X.S., Zhou, X.M., 2002. Zircon chemistry and magma mixing, SE China: in-situ analysis of Hf isotopes, Tonglu and Pingtan igneous complexes. Lithos 61, 237–269.

Halama, R., Waight, T.E., Markl, G., 2002. Geochemical and isotopic zoning patterns of plagioclase megacrysts in gabbroic dykes from the Gardar Province, South Greenland: implications for crystallization processes in anorthositic magmas. Contributions to Mineralogy and Petrology 144, 109–127.

Holden, P., Halliday, A.N., Stepens, W.E., 1987. Neodymium and strontium isotope content of microdiorite enclaves points to mantle input to granitoid production. Nature 330, 53–56.

Hou, M.L., Jiang, Y.H., Jiang, S.Y., Ling, H.F., Zhao, K.D., 2007. Contrasting origins of late Mesozoic adakitic granitoids from the northwestern Jiaodong Peninsula, east China: implications for crustal thickening to delamination. Geological Magazine 144, 619–631.

Jahn, B.M., Wu, F.Y., Lo, C.H., Tsai, C.H., 1999. Crust–mantle interaction induced by deep subduction of the continental crust: geochemical and Sr–Nd isotopic evidence from post-collisional mafic–ultramafic intrusions of the northern Dabie complex, central China. Chemical Geology 157, 119–146.

Jahn, B.M., Liu, D.Y., Wan, Y.S., Song, B., Wu, J.S., 2008. Archean crust evolution of the Jiaodong Peninsula, China, as revealed by zircon SHRIMP geochronology,

element and Nd-isotope geochemistry. American Journal of Science 308, 232–269.
Knesel, K.M., Davidson, J.P., Duffield, W.A., 1999. Evolution of silicic magma through assimilation and subsequent recharge: evidence from Sr-isotopes in sanidine phenocrysts, Taylor Creek Rhyolite, NM. Journal of Petrology 40, 773–786.
Kumar, S., Rino, V., 2006. Mineralogy and geochemistry of microgranular enclaves in Palaeoproterozoic Malanjkhand granitoids, central India: evidence of magma mixing, mingling, and chemical equilibration. Contributions to Mineralogy and Petrology 152, 591–609.
Langmuir, C.H., Vocke, R.D., Hanson, G.N., 1978. A general mixing equation with applications to Icelandic basalts. Earth and Planetary Science Letters 37, 380–392.
Lee, M.R., Parsons, I., 1997. Dislocation formation and albitization in alkali feldspars from the Shap granite. American Mineralogist 82, 557–570.
Lesher, C.E., 1990. Decoupling of chemical and isotopic exchange during magma mixing. Nature 344, 235–237.
Lesher, C.E., 1994. Kinetics of Sr and Nd exchange in silicate liquids: theory, experiments, and applications to uphill diffusion, isotopic equilibration, and irreversible mixing of magmas. Journal of Geophysical Research 99, 9585–9604.
Liu, J., Davis, G.A., Lin, Z., Wu, F.Y., 2005. The Liaonan metamorphic core complex, Southeastern Liaoning Province, North China: a likely contributor to Cretaceous rotation of Eastern Liaoning, Korea and contiguous areas. Tectonophysics 407, 65–80.
Liu, Y.S., Hu, Z.C., Gao, S., Günther, D., Xu, J., Gao, C.G., Chen, H.H., 2008. In situ analysis of major and trace elements of anhydrous minerals by LA-ICP-MS without applying an internal standard. Chemical Geology 257, 34–43.
Liu, S., Hu, R., Gao, S., Feng, C.X., Yu, B., Feng, G., Qi, Y.Q., Wang, T., Coulson, I.M., 2009. Petrogenesis of Late Mesozoic mafic dykes in the Jiaodong Peninsula, eastern North China Craton and implications for the foundering of lower crust. Lithos 13, 621–639.
Liu, Y.S., Gao, S., Hu, Z.C., Gao, C.G., Zong, K., Wang, D., 2010. Continental and oceanic crust recycling-induced melt–peridotite interactions in the Trans-North China Orogen: U–Pb dating, Hf isotopes and trace elements in zircons of mantle xenoliths. Journal of Petrology 51, 537–571.
Ludwig, K.R., 2003. User's Manual for Isoplot 3.00, a Geochronolgical Toolkit for Microsoft Excel. Berkeley Geochronological Center Special Publication No. 4, pp. 25–32.
Lugmair, G.W., Harti, K., 1978. Lunar initial $^{143}Nd/^{144}Nd$: differential evolution of the lunar crust and mantle. Earth and Planetary Science Letters 39, 349–357.
Martin, V.M., Davidson, J.P., Morgan, D.J., Jerram, D.A., 2010. Using the Sr isotope compositions of feldspars and glass to distinguish magma system components and dynamics. Geology 38, 539–542.
Means, W.D., Park, Y., 1994. New experimental approach to understanding igneous texture. Geology 22, 323–326.
Meng, Q.R., 2003. What drove late Mesozoic extension of the northern China–Mongolia tract? Tectonophysics 369, 155–174.
Menzies, M.A., Xu, Y.G., Zhang, H.F., Fan, W.M., 2007. Integration of geology, geophysics and geochemistry: a key to understanding the North China Craton. Lithos 96, 1–21.
Michard, A., 1989. Rare earth element systematics in hydrothermal fluids. Geochimica et Cosmochimica Acta 53, 745–750.
Middlemost, E.A.K., 1994. Naming materials in the magma/igneous rock system. Earth Science Reviews 74, 193–227.
Morgan, D.J., Jerram, D.A., Chetkoff, D.G., Davidson, J.P., Pearson, D.G., Kronz, A., Nowell, G.M., 2007. Combining CSD and isotopic microanalysis: magma supply and mixing processes at Stromboli volcano, Aeolian Islands, Italy. Earth and Planetary Science Letters 260, 419–431.
Parsons, I., Lee, M.R., 2009. Mutual replacement reactions in alkali feldspars I: microtextures and mechanisms. Contributions to Mineralogy and Petrology 157, 641–661.
Perini, G., Tepley III, F.J., Davidson, J.P., Conticelli, S., 2003. The origin of K-feldspar megacrysts hosted in alkaline potassic rocks from central Italy: a track for low-pressure processes in mafic magmas. Lithos 66, 223–240.
Piwinskii, A.J., 1968. Experimental studies of igneous rock series, central Sierra Nevada Batholith, Californa. Journal of Geology 76, 548–570.
Ramos, F.C., Tepley, F.J.I.I.I., 2008. Inter- and Intra-crystalline Isotopic disequilibria: techniques and applications. Reviews in Mineralogy and Geochemistry 69, 403–443.
Siebel, W., Reitter, E., Wenzel, T., Blaha, U., 2005. Sr isotope systematics of K-feldspars in plutonic rocks revealed by the Rb–Sr microdrilling technique. Chemical Geology 222, 183–199.
Söderlund, U., Patchett, P.J., Vervoort, J.D., Isachsen, C.E., 2004. The ^{176}Lu decay constant determined by Lu–Hf and U–Pb isotope systematics of Precambrian mafic intrusions. Earth and Planetary Science Letters 219, 311–324.
Sun, S.S., McDonough, W.F., 1989. Chemical and isotopic systematics of oceanic basalts: implications for mantle composition and processes. In: Saunders, A.D., Norry, M.J. (Eds.), Magmatism in the Oceanic Basalts. Geological Society Special Publication, pp. 313–345.
Sun, W.D., Ding, X., Hu, Y.H., Li, X.H., 2007. The golden transformation of the Cretaceous plate subduction in the west Pacific. Earth and Planetary Science Letters 262, 533–542.
Tam, P.K., Zhao, G.C., Liu, F., Zhou, X., Sun, M., Li, S.Z., 2011. Timing of metamorphism in the Paleoproterozoic Jiao-Liao-Ji Belt: new SHRIMP U–Pb zircon dating of granulites, gneisses and marbles of the Jiaobei massif in the North China Craton. Gondwana Research 19, 150–162.
Tang, J., Zheng, Y.F., Wu, Y.B., Gong, B., Liu, X.M., 2007. Geochronology and geochemistry of metamorphic rocks in the Jiaobei terrane: constraints on its tectonic affinity in the Sulu orogen. Precambrian Research 152, 48–82.
Tepley III, F.J., Davidson, J.P., 2003. Mineral-scale Sr-isotope constraints on magma evolution and chamber dynamics in the Rum layered intrusion, Scotland. Contributions to Mineralogy and Petrology 145, 628–641.
Tepley III, F.J., Davidson, J.P., Clynne, M.A., 1999. Magmatic interactions as recorded in plagioclase phenocrysts of Chaos Crags, Lassen Volcanic Center, California. Journal of Petrology 40, 787–806.
Tepley III, F.J., Davidson, J.P., Tilling, R.I., Arth, J.G., 2000. Magma mixing, recharge and eruption histories recorded in plagioclase phenocrysts from El Chichón volcano, Mexico. Journal of Petrology 41, 1397–1411.
Van Orman, J.A., Grove, T.L., Shimizu, N., 2001. Rare earth element diffusion in diopside: influence of temperature, pressure, and ionic radius, and an elastic model for diffusion in silicates. Contributions to Mineralogy and Petrology 141, 687–703.
Vernon, R.H., 1984. Microgranitoid enclaves: globules of hybrid magma quenched in a plutonic environment. Nature 304, 438–439.
Waight, T.E., Maas, R., Nicholls, I.A., 2000. Fingerprinting feldspar phenocrysts using crystal isotopic composition stratigraphy: implications for crystal transfer and magma mingling in S-type granites. Contributions to Mineralogy and Petrology 139, 227–239.
Waight, T.E., Maas, R., Nicholls, I.A., 2001. Geochemical investigations of microgranitoid enclaves in the S-type Cowra Granodiorite, Lachlan Fold Belt, SE Australia. Lithos 56, 165–186.
Wan, Y.S., Song, B., Liu, D.Y., Wilde, S.A., Wu, J.S., Shi, Y.R., Yin, X.A., Zhou, H.Y., 2006. SHRIMP zircon geochronology of Paleoproterozoic metasedimentary rocks in the North China Craton: evidence for a major late Paleoproterozoic tectonothermal event. Precambrian Research 149, 249–271.
Wang, L.G., Qiu, Y.M., McNaughton, N.J., Groves, D.I., Luo, Z.K., Huang, J.Z., Miao, L.C., Liu, Y.K., 1998. Constraints on crustal evolution and gold metallogeny in the Northwestern Jiaodong Peninsula, China, from SHRIMP U–Pb zircon studies of granitoids. Ore Geology Reviews 13, 275–291.
Whitney, J.A., 1975. The effects of pressure, temperature, and X_{H2O} on phase assemblages in four synthetic rock compositions. Journal of Geology 83, 1–31.
Wiedenbeck, M., Alle, P., Corfu, F., Griffin, W.L., Meier, M., Oberli, F., Quadt, A.V., Roddick, J.C., Spiegel, W., 1995. Three natural zircon standards for U–Th–Pb, Lu–Hf, trace element and REE analyses. Geostandards and Geoanalytical Research 19, 1–23.
Worden, R.H., Walker, D.L., Parsons, I., Brown, W.L., 1990. Development of microporosity, diffusion channels and deuteric coarsening in perthitic alkali feldspars. Contributions to Mineralogy and Petrology 104, 507–515.
Wu, F.Y., Lin, J.Q., Wilde, S.A., Zhang, X.O., Yang, J.H., 2005a. Nature and significance of the Early Cretaceous giant igneous event in eastern China. Earth and Planetary Science Letters 233, 103–119.
Wu, F.Y., Zhao, G.C., Wilde, S.A., Sun, D.Y., 2005b. Nd isotopic constraints on the crustal formation of the North China Craton. Journal of Asian Earth Science 24, 523–545.
Wyllie, P.J., Cox, K.G., Biggar, G.M., 1962. The habit of apatite in synthetic systems and igneous rocks. Journal of Petrology 3, 238–243.
Xie, L.W., Zhang, Y.B., Sun, J.F., Wu, F.Y., 2008. In situ simultaneous determination of trace elements, U–Pb and Lu–Hf isotopes in zircon and baddeleyite. Chinese Science Bulletin 53, 1565–1573.
Xu, Y.G., 2007. Diachronous lithospheric thinning of the North China Craton and formation of the Daxin'anling–Taihangshan gravity lineament. Lithos 96, 281–298.
Xu, Y.G., Ma, J.L., Huang, X.L., Iizuka, Y., Chung, S.L., Wang, Y.B., Wu, X.Y., 2004. Early Cretaceous gabbroic complex from Yinan, Shandong Province: petrogenesis and mantle domains beneath the North China Craton. International Journal of Earth Sciences 93, 1025–1041.
Xu, Y.G., Li, H.Y., Pang, C.J., He, B., 2009. On the timing and duration of the destruction of the North China Caton. Chinese Science Bulletin 54, 3379–3396.
Yan, J., Chen, J.F., Xie, Z., Zhou, T.X., 2003. Mantle xenoliths from Late Cretaceous basalt in eastern Shandong Province: new constraint on the timing of lithospheric thinning in eastern China. Chinese Science Bulletin 48, 2139–2144.
Yang, J.H., Wu, F.Y., Chung, S.L., Wilde, S.A., Chu, M.F., 2004a. Multiple sources for the origin of granites: geochemical and Nd/Sr isotopic evidence from the Gudaoling granite and its mafic enclaves, northeast China. Geochimica et Cosmochimica Acta 68, 4469–4483.
Yang, J.H., Chung, S.L., Zhai, M.G., Zhou, X.H., 2004b. Geochemical and Sr–Nd–Pb isotopic compositions of mafic dikes from the Jiaodong Peninsula, China: evidence for vein-plus-peridotite melting in the lithospheric mantle. Lithos 73, 145–160.
Zhai, M.G., Santosh, M., 2011. The Early Precambrian odyssey of the North China Craton: a synoptic overview. Gondwana Research 20, 6–25.
Zhang, H.F., Sun, M., Zhou, X.H., Fan, W.M., Zhai, M.G., Yin, J.F., 2002. Mesozoic lithosphere destruction beneath the North China Craton: evidence from major-, trace-element and Sr–Nd–Pb isotope studies of Fangcheng basalts. Contributions to Mineralogy and Petrology 144, 241–253.
Zhang, H.F., Sun, M., Zhou, X.H., Zhou, M.F., Fan, W.M., Zheng, J.P., 2003. Secular evolution of the lithosphere beneath the eastern North China Craton: evidence from Mesozoic basalts and high-Mg andesites. Geochimica et Cosmochimica Acta 67, 4373–4387.
Zhang, J., Zhang, H.F., Ying, J.F., Tang, Y.J., Niu, L.F., 2008. Contribution of subducted Pacific slab to Late Cretaceous mafic magmatism in Qingdao region, China: a petrological record. Island Arc 17, 231–241.

Zhang, J., Zhao, Z.F., Zheng, Y.F., Dai, M.N., 2010. Postcollisional magmatism: Geochemical constraints on the petrogenesis of Mesozoic granitoids in the Sulu orogen, China. Lithos 119, 512–536.

Zhang, H.F., Ying, J.F., Tang, Y.J., Li, X.H., Feng, C., Santosh, M., 2011. Phanerozoic reactivation of the Archean North China Craton through episodic magmatism: evidence from zircon U–Pb geochronology and Hf isotopes from the Liadong Peninsula. Gondwana Research 19, 446–459.

Zhao, G.C., Wilde, S.A., Cawood, P.A., Lu, L., 1998. Thermal evolution of Archaean basement rocks from the Eastern part of the North China Craton and its bearing on tectonic setting. International Geology Review 40, 706–721.

Zhao, G.C., Wilde, S.A., Cawood, P.A., Sun, M., 2001. Archean blocks and their boundaries in the North China Craton: lithological, geochemical, structural and P–T path constraints and tectonic evolution. Precambrian Research 107, 45–73.

Zhu, G., Song, C.Z., Wang, D.X., Liu, G.S., Xu, J.W., 2001. Studies on $^{40}Ar/^{39}Ar$ thermochronology of strike-slip time of the Tan-Lu fault zone and their tectonic implications. Science in China (Earth Sciences) 44, 1002–1009.

Zindler, A., Staudigel, H., Batiza, R., 1984. Isotope and trace element geochemistry young Pacific seamounts: implications for the scale of upper mantle heterogeneity. Earth and Planetary Science Letters 70, 175–195.